

# **Mesoscopic three-dimensional hard X-ray imaging of central and peripheral nervous system**

**Inauguraldissertation**  
zur  
Erlangung der Würde eines Doktors der Philosophie  
vorgelegt der  
Philosophisch-Naturwissenschaftlichen Fakultät  
der Universität Basel

von

Christos Bikis  
aus Athen, Griechenland

2019

Genehmigt von der Philosophisch-Naturwissenschaftlichen Fakultät

auf Antrag von:

Prof. Dr. Bert Müller, Fakultätsverantwortlicher  
Prof. Dr. Alex Dommann, Korreferent

Basel, den 12. Dezember 2017

Prof. Dr. Martin Spiess, Dekan

# Contents

<b>Summary</b>	<b>v</b>
<b>Zusammenfassung</b>	<b>vii</b>
<b>List of Publications</b>	<b>ix</b>
<b>1 Introduction</b>	<b>1</b>
<b>2 Results</b>	<b>5</b>
2.1 Sensitivity comparison of absorption and grating-based phase tomography of paraffin-embedded human brain tissue . . . . .	5
2.2 Three-dimensional and non-destructive characterization of nerves inside conduits using laboratory-based micro computed tomography . .	11
2.3 Three-dimensional imaging and analysis of entire peripheral nerves after repair and reconstruction . . . . .	33
<b>3 Conclusions</b>	<b>57</b>
<b>Bibliography</b>	<b>60</b>
<b>Acknowledgements</b>	<b>61</b>
<b>Curriculum Vitae</b>	<b>65</b>



## Summary

Micro computed tomography ( $\mu$ CT), either by means of hard X rays from synchrotron radiation (SR) facilities, or from advanced laboratory sources, has been proven as a powerful method for the nondestructive three-dimensional visualization of biological specimens with isotropic micro- and even nanometer resolution. The established absorption-contrast modality of  $\mu$ CT has been sometimes associated with the need for contrast agents, whereas the more advanced phase-contrast modality has yielded superior results for biological specimens without staining. For around three decades, phase-contrast  $\mu$ CT has been considered between a hundred and a thousand times better than absorption-contrast  $\mu$ CT, based on the ratio of the imaginary and the real part of the complex refractive index that could be determined using the two modalities at desired photon energies.

The results of the present study elucidate that for formalin-fixed, paraffin-embedded nervous tissues, conventional  $\mu$ CT delivers a much better contrast than originally expected. Related measurements were performed at a SR facility using monochromatic X rays. The photon energies were not equal for absorption- and phase-contrast measurements, but selected to obtain optimized contrast within a reasonable period of time. The choice of the photon energy, which is much smaller for absorption-contrast  $\mu$ CT, explains that the contrast difference between phase- and absorption-contrast  $\mu$ CT, indicated by the contrast-to-noise ratio of anatomical regions in the respective datasets being about two times better for phase  $\mu$ CT, is much smaller than reported in literature.

It should be highlighted that  $\mu$ CT in absorption- and phase contrast are complementary methods and a combination might give additional quantitative insights into the three-dimensional images. For example, one can register the data and build a joint histogram from the common volume to segment anatomical features indistinguishable using just one imaging modality. The main relevance of such results lies in the opportunity to employ laboratory-based  $\mu$ CT, which are much better accessible and cost-effective than  $\mu$ CT at SR facilities.

This approach was benchmarked on peripheral nerve reconstruction. The three-dimensional visualization of regenerating nerves inside collagen scaffolds was feasible and included the automatic extraction of anatomical features to quantify the regeneration. Indeed, the characteristic parameters, revealed from the conventional  $\mu$ CT data, were significantly different between regenerating and control nerves. The approach including specimen preparation, data acquisition, and analysis has been useful for the investigations of the anatomical alterations in medial temporal epilepsy and the time-critical diagnosis of vasculitis prior to the standard histology.



# Zusammenfassung

Mikrotomographie ( $\mu$ CT) nutzt harte Röntgenstrahlen von Synchrotronstrahlungsquellen oder hochgezüchteten Laborquellen. Die  $\mu$ CT ist eine leistungsfähige Methode für die zerstörungsfreie dreidimensionale Bildgebung biologischer Proben mit Mikrometer- oder sogar Nanometerauflösung. Der etablierte Absorptionskontrast bei Weichgeweben basiert oft auf Kontrastmedien, während fortschrittliche Phasenmethoden ausgezeichneten Kontrast in biologischen Geweben auch ohne spezielle Marker liefern. Seit drei Jahrzehnten ist in der Literatur beschrieben, dass Phasenkontrast einen hundert oder sogar tausendfach besseren Kontrast liefern solle, weil der Real- den Imaginär-Teil des Brechungsindex etwa um drei Größenordnungen übersteigt.

Die Ergebnisse der vorliegenden Arbeit zeigen, dass die Absorption für Formalinfixiertes und in Paraffin eingebettetes Nervengewebe einen besseren Kontrast als erwartet liefert. Entsprechende Messungen an einer Synchrotronstrahlungsquelle mit monochromatischen Röntgenstrahlen wurden durchgeführt. Die Photonenergien waren dabei nicht gleich, sondern so gewählt, dass man einen optimierten Kontrast innerhalb der begrenzten Messzeit erhalten hat. Die Photonenergie, die für den konventionellen Absorptionskontrast deutlich niedriger war, kann herangezogen werden, um zu erklären, warum der Kontrastunterschied deutlich kleiner als in der Literatur vorhergesagt, ist. Anhand der Kontrastempfindlichkeit der verschiedenen Gewebe kann man schlussfolgern, dass der Phasenkontrast gegenüber dem Absorptionskontrast doppelt so gut ist.

Es soll hervorgehoben werden, dass Absorption und Phase komplementär sind und eine Kombination deshalb zusätzliche Einblicke in die dreidimensionalen Daten liefern kann. Beispielsweise kann man die Phasen- und Absorptions-Tomogramme in ein Koordinatensystem überführen und aus dem gemeinsamen Volumen ein gemeinsames Histogramm erzeugen. Dieses Histogramm erlaubt dann die Segmentierung von anatomischen Regionen, die mit einer Methode allein schwer oder gar nicht zugänglich sind. Die Relevanz der Ergebnisse liegt hauptsächlich in der Möglichkeit die Messungen anstatt an Synchrotronstrahlungsquellen an den besser zugänglichen und preislich günstigen Laborquellen zu erhalten.

Der vorgeschlagene Weg wurde für periphere Nervenregeneration aufgezeigt. So konnte man den Nerv innerhalb eines Kollagenzyinders mittels  $\mu$ CT sichtbar machen. Die Qualität der dreidimensionalen Bilder ermöglichen eine automatische Bestimmung anatomischer Charakteristika, um die Regeneration zu quantifizieren. Der Unterschied zwischen einem regenerierten Nerv und der gesunden Kontrolle wurde klar nachgewiesen. Dieses Vorgehen, einschliesslich Probenpräparation, Datenaufnahme und Analyse, war auch für die Visualisierung der anatomischen Veränderungen durch Epilepsie und für die zeitkritische Diagnose der Vasculitis vor der Histologie erfolgreich.



## List of Publications

**C. Bikis**, G. Rodgers, H. Deyhle, P. Thalmann, A. Hipp, F. Beckmann, T. Weitkamp, S. Theocharis, C. Rau, G. Schulz and B. Müller, “*Sensitivity comparison of absorption and grating-based phase tomography of paraffin-embedded human brain tissue*”, Applied Physics Letters, 114, 083702 (2019).

DOI:10.1063/1.5085302

G. Rodgers, G. Schulz, H. Deyhle, S. Marathe, **C. Bikis**, T. Weitkamp and B. Müller, “*A quantitative correction for phase wrapping artifacts in hard X-ray grating interferometry*”, Applied Physics Letters, 113, 093702 (2018).

DOI:10.1063/1.5045398

H. Deyhle, **C. Bikis**, A. Khimchenko, G. Schweighauser, J. Hench, G. Schulz, B. Müller and S. E. Hieber, “*Visualization and segmentation of cells in unstained paraffin-embedded cerebral tissue*”, Microscopy and Microanalysis, 24 (Suppl 2), 408 (2018).

DOI:10.1017/S1431927618014320

A. Khimchenko, A. Pacureanu, **C. Bikis**, S. E. Hieber, P. Thalmann, H. Deyhle, G. Schweighauser, J. Hench, S. Frank, M. Müller-Gerbl, G. Schulz, P. Cloetens and B. Müller, “*Hard X-ray nano-holotomography of formalin-fixed and paraffin-embedded human brain tissue*”, Microscopy and Microanalysis, 24 (Suppl 2), 354 (2018).

DOI:10.1017/S143192761801406X

A. Khimchenko, **C. Bikis**, A. Pacureanu, S. E. Hieber, P. Thalmann, H. Deyhle, G. Schweighauser, J. Hench, S. Frank, M. Müller-Gerbl, G. Schulz, P. Cloetens and B. Müller, “*Hard X-ray nano-holotomography: Large-scale, label-free, three-dimensional neuroimaging beyond optical limit*”, Advanced Science, 5(6), 1700694 (2018).

DOI:10.1002/advs.201700694

N. Chicherova, S. E. Hieber, A. Khimchenko, **C. Bikis**, B. Müller and P. Cattin, “*Automatic deformable registration of histological slides to  $\mu$ CT volume data*”, Journal of Microscopy, 217(1), 49 (2018).

DOI:10.1111/jmi.12692

**C. Bikis**, P. Thalmann, L. Degruillier, G. Schulz, B. Müller, D. F. Kalbermatten, S. Madduri, and S. E. Hieber, “*Three-dimensional and non-destructive characterization of nerves inside conduits using laboratory-based micro computed tomography*”, Journal of Neuroscience Methods, 294, 59 (2018).

DOI:10.1016/j.jneumeth.2017.11.005

**C. Bikis**, L. Degruillier, P. Thalmann, G. Schulz, B. Müller, S. E. Hieber, D. F. Kalbermatten, and S. Madduri, “*Three-dimensional imaging and analysis of*

*entire peripheral nerves after repair and reconstruction*”, Journal of Neuroscience Methods, 295, 37 (2018).  
DOI:10.1016/j.jneumeth.2017.11.015

P. Thalmann, **C. Bikis**, A. Hipp, B. Müller, S. E. Hieber, and G. Schulz, “*Single and double grating-based X-ray microtomography using synchrotron radiation*”, Applied Physics Letters, 110, 061103 (2017).

P. Thalmann, **C. Bikis**, G. Schulz, P. Paleo, A. Mirone, A. Rack, and B. Müller, “*Removing ring artefacts from synchrotron radiation-based hard X-ray tomography data*”, Proceedings of SPIE, 10391, 1039114 (2017).

A. Khimchenko, G. Schulz, **C. Bikis**, H. Deyhle, N. Chicherova, S. E. Hieber, G. Schweighauser, J. Hench and B. Müller, “*Three-dimensional imaging of human brain tissues using absorption-contrast high-resolution X-ray tomography*”, Proceedings of SPIE, 10162, 101620K (2017).

A. Khimchenko, **C. Bikis**, G. Schweighauser, J. Hench, A.-T. Joita-Pacureanuc, P. Thalmann, H. Deyhle, B. Osmani, N. Chicherova, S. E. Hieber, P. Cloetens, M. Müller-Gerbl, G. Schulz, and B. Müller, “*Imaging cellular and subcellular structure of human brain tissue using micro computed tomography*”, Proceedings of SPIE, 10391, 103910K (2017).

A. Khimchenko, **C. Bikis**, G. Schulz, M-C. Zdora, I. Zanette, J. Vila-Comamala, G. Schweighauser, J. Hench, S. E. Hieber, H. Deyhle, P. Thalmann, and B. Müller, “*Hard X-ray submicrometer tomography of human brain tissue at Diamond Light Source*”, Journal of Physics: Conference Series, 849, 012030 (2017).

N. Chicherova, S. E. Hieber, G. Schulz, A. Khimchenko, **C. Bikis**, P. Cattin and B. Müller, “*Automatic histology registration in application to X-ray modalities*”, Proceedings of SPIE, 9967, 996708 (2016).

S. E. Hieber, **C. Bikis**, A. Khimchenko, G. Schweighauser, J. Hench, N. Chicherova, G. Schulz and B. Müller, “*Tomographic brain imaging with nucleolar detail and automatic cell counting*”, Scientific Reports, 6, 32156 (2016).

A. Khimchenko, H. Deyhle, G. Schulz, G. Schweighauser, J. Hench, N. Chicherova, **C. Bikis**, S. E. Hieber and B. Müller, “*Extending two-dimensional histology into the third dimension through conventional micro computed tomography*”, NeuroImage, 139, 26 (2016).

A. Khimchenko, G. Schulz, H. Deyhle, S. E. Hieber, S. Hasan, **C. Bikis**, J. Schulz, L. Costeur and B. Müller, “*Non-destructive phase contrast hard X-ray imaging to reveal the three-dimensional microstructure of soft and hard tissues*”, Proceedings of SPIE, 9797, 97970B (2016).

A. Khimchenko, G. Schulz, H. Deyhle, P. Thalmann, I. Zanette, M-C. Zdora, **C. Bikis**, A. Hipp, S. E. Hieber, G. Schweighauser, J. Hench, and B. Müller, “*X-ray micro-tomography for investigations of brain tissues on cellular level*”, Proceedings of SPIE, 9967, 996703 (2016).

**C. Bikis**, P. Janz, G. Schulz, G. Schweighauser, J. Hench, P. Thalmann, H. Deyhle, N. Chicherova, A. Rack, A. Khimchenko, S. E. Hieber, L. Mariani, C. A. Haas, and B. Müller, “*High-resolution synchrotron radiation-based phase tomography of the healthy and epileptic brain*”, Proceedings of SPIE, 9967, 996706 (2016).

H. Deyhle, G. Schulz, A. Khimchenko, **C. Bikis**, S. E. Hieber, C. Jaquierey, C. Kunz, M. Müller-Gerbl, S. Höchel, T. Saxon, A. K. Stalder, B. Ilgenstein, F. Beckmann, P. Thalmann, M. Buscema, N. Rohr, M. N. Holme, and B. Müller, “*Imaging tissues for biomedical research using the high-resolution micro-tomography system nanotom®m*”, Proceedings of SPIE, 9967, 99670Q (2016).

S. E. Hieber, **C. Bikis**, A. Khimchenko, G. Schulz, H. Deyhle, P. Thalmann, N. Chicherova, A. Rack, M-C. Zdora, I. Zanette, G. Schweighauser, J. Hench, and B. Müller, “*Computational cell quantification in the human brain tissues based on hard X-ray phase-contrast tomograms*”, Proceedings of SPIE, 9967, 99670K (2016).

A. Khimchenko, G. Schulz, I. Zanette, M.-C. Zdora, A. Hipp, H. Deyhle, S. E. Hieber, **C. Bikis**, G. Schweighauser, J. Hench, P. Thalmann, and B. Müller, “*Single grating X-ray phase-contrast tomography for evaluation of brain tissue degeneration on cellular level*”, European Cells and Materials, 32 Supplement 2, 41 (2016).

**C. Bikis**, L. Degruillier, H. Deyhle, G. Schulz, G. Schweighauser, J. Hench, B. Müller, S. Madduri, S. E. Hieber, “*Using laboratory μCT for assessing peripheral nerve regeneration*”, European Cells and Materials, 32 Supplement 2, 30 (2016).

**C. Bikis**, G. Schweighauser, J. Hench, G. Schulz, B. Müller, S. E. Hieber, “*Phase tomography as a three-dimensional complement to histology for nervous tissue visualization*”, Pathologe, 36, 62 (2015).

**C. N. Bikis**, G. Schulz, B. Müller and S. E. Hieber, “*Histology-validated, phase-contrast tomography for visualizing the cerebellum*”, European Cells and Materials, 30 Supplement 1, 21 (2015).

S. E. Hieber, **C. N. Bikis**, A. Khimchenko, G. Schulz, G. Schweighauser, J. Hench, and B. Müller, “*Three-dimensional imaging of brain tissue by grating-based micro computed tomography using synchrotron radiation*”, European Cells and Materials, 30 Supplement 1, 44 (2015).



# 1 Introduction

In terms of imaging and morphological analysis, the nervous system presents medical practitioners and researchers with considerable challenges. The brain, being completely enclosed inside the skull, is more difficult to image and access than most organs, especially *in vivo*. Furthermore, biopsies of the nervous system must be kept at an absolute minimum both in terms of frequency as well as with regard to the size of the extracted tissue sample, given the limited choices of viable biopsy sites and the inherently low regenerative capacity of the nervous system. To achieve true and sub-micrometer resolution, investigation under the optical or electron microscopes is the widely established practice, both in a clinical setting, as well as in animal experiments. To complement these two destructive methods, micro computed tomography ( $\mu$ CT), both by means of laboratory sources and synchrotron radiation (SR), is the prime candidate. It can usually be performed prior to any desired step of the histological processing, not affecting the subsequent workup, while offering isotropic resolution at the micrometer and even nanometer scale.

Apart from the conventional absorption-contrast mode,  $\mu$ CT can also be performed in the phase-contrast mode, first proposed in 1965 by Bonse and Hart [1]. For light elements, that biological tissues mainly consist of, and photon energies at the order of 10 keV, the real part of the refractive index is three orders of magnitude larger than the imaginary one [2]. Based on this difference, researchers estimated that phase-contrast  $\mu$ CT is a hundred, if not a thousand times more sensitive than absorption-contrast  $\mu$ CT [3–5].

In the last three decades,  $\mu$ CT has been used extensively and has revolutionized several aspects of biomedical research. Such pioneering works related to the field of neurosciences, that have also motivated this work, will be mentioned in what follows. In 1995, phase-contrast radiographs of rat cerebellum manifested the superior contrast offered by phase tomography to visualize the nervous tissue, which exhibits a relatively low X-ray absorption [2]. In 1999, visualization of the rat trigeminal nerves by means of phase tomography has revealed the consistent performance of the phase-contrast modality in visualizing not only the central, but also the peripheral nervous system. Nearly a decade later, SR phase micro CT has lead to the visualization of intact neuronal Purkinje cells in formalin-fixed human cerebellum [6]. This was the first time an intact neuronal cell has been visualized without the use of a contrast agent inside its surrounding tissue and opened the possibility of cell counting and studies of neuronal density in a three-dimensional tissue volume, avoiding the need for contrast agents or specimen sectioning.

Nevertheless, phase tomography generally requires more expensive and delicate instrumentation, as well as a significant level of technical expertise. Hence, micro tomography in the established absorption-contrast has been used extensively for

visualizing the nervous system. By means of osmium staining, cell counting of neurons inside the inner ear was possible [7]. To visualize the neuronal bodies inside the intact, thick and high-absorbing petrosal bone, osmium staining was employed. An analogous approach, based on the combination of contrast agent and high resolution absorption-contrast micro CT was employed for the visualization of the rat sciatic nerve vasculature [8]. The use of contrast agents though is associated with technical challenges and after the tomographic measurement, any subsequent histological processing becomes more complex. This is why our group, together with the collaborating Neuropathology Department of Basel University has considered the use of formalin-fixed, paraffin embedded (FFPE) specimens for  $\mu$ CT measurements, with the rationale of both increasing absorption contrast by the increase in density that follows tissue dehydration, as well as retaining compatibility with the established histological processing.

Based on the above considerations, this work aims to answer four main questions: (a) Could paraffin embedding indeed lead to increased visualization quality by means of absorption  $\mu$ CT for nervous tissues, compared to aqueous (e.g. formalin) solutions? (b) Is phase-contrast tomography a hundred to a thousand times better than absorption-contrast for nervous tissue, as one may expect, or is the gap smaller in experimental conditions? (c) Given the fact that the two modalities describe complementary physical quantities, could they be employed in tandem, to yield more information for a given specimen? (d) What are the clinical and biomedical challenges that can be addressed by using the widely employed laboratory micro CT systems to investigate readily available FFPE specimens?

In 2016, we have reported the visualization of neuronal sub-cellular details, namely nucleus and nucleolus of the Purkinje cells, in FFPE human cerebellum specimens, by means of SR $\mu$ CT [9]. Owing to both the spatial resolution, as well as the high contrast of the presented datasets, automatic cell counting was also possible and we have also proposed a number of biomedical and clinical applications where such an approach could be applied. During the same year and again while investigating FFPE human cerebellum samples without any contrast agent, we were able to visualize individual Purkinje cells by means of conventional absorption-contrast  $\mu$ CT using a commercial laboratory X-ray system [10]. Given the fact that such systems are more readily available, considerably easier to operate and exceedingly more cost- and time-effective compared to SR experiments, this finding was deemed an important milestone in the three-dimensional visualization of nervous tissue by means of X rays.

To further investigate the above results in a quantitative way, synchrotron-radiation experiments were performed as part of this study, directly correlating phase- and absorption-contrast  $\mu$ CT results of FFPE brain tissue. Human cerebellum samples were provided by S. Theocharis from the Department of Pathology, University of Athens. A selected sample was measured at the P05 beamline of the DESY Synchrotron in Hamburg, Germany, as well as the Diamond Manchester Imaging Beamline I13-2 of the Diamond Light Source in Didcot, UK, with the valuable help of the beamline scientists F. Beckmann and A. Hipp, and C. Rau, respectively, which were also involved in the tomographic reconstruction of the obtained projections. To account for phase wrapping artifacts, an algorithm developed by T. Weitkamp

---

of the Synchrotron Soleil, Gif-sur-Yvette, France, was used. Our group members B. Müller, G. Schulz and G. Rodgers have participated in the synchrotron measurements and contributed to the data processing, tomographic reconstruction and analysis. For these last three tasks, P. Thalmann was also actively involved. The support of our group member W. Kuo, as well as S. Marathe of the Diamond Light Source during the measurements should also be mentioned. A. Scherberich from the Department of Biomedicine, University Hospital Basel has provided materials needed for the specimen preparation. The histological equipment was provided by S. Frank and J. Hench of the Neuropathology Department, University Hospital Basel.

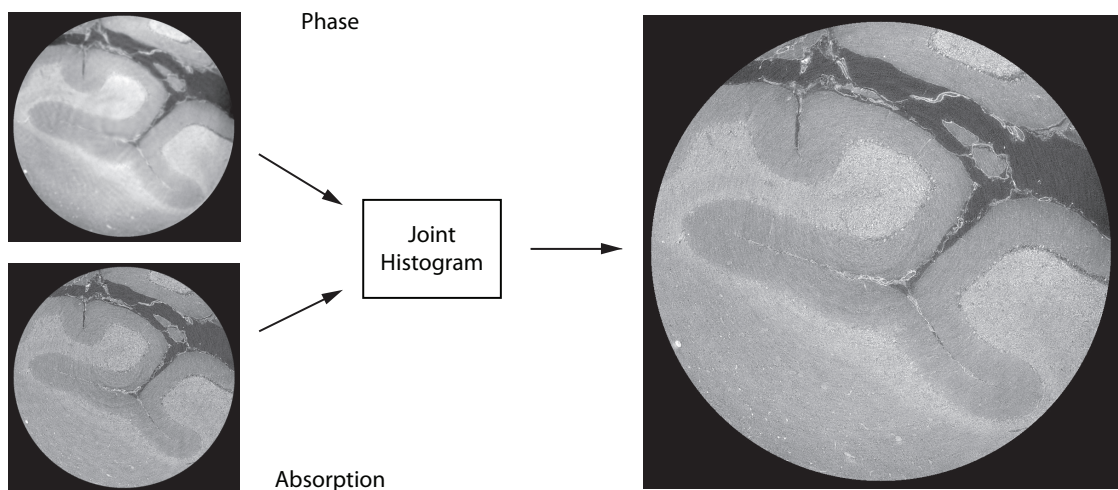
The second part of the work presented here focused, as already mentioned, on the practical application of  $\mu$ CT visualization of FFPE nervous tissue, and namely the quantitative characterization of peripheral nerves after repair and reconstruction by means of biodegradable scaffolds. This application was chosen based on the considerable significance of peripheral nerve injuries. Several hundred thousand new patients are affected annually [11] and the socio-economical burden associated with work leave, health care expenses and chronic disability is substantial [12]. The current therapeutic interventions of choice are end-to-end suturing and autologous nerve grafting [13,14], both related to considerable shortcomings, with the functional outcome often being unsatisfactory. In detail, end-to-end suturing is associated with reduced stretching capacity in approximately 25% of the cases, due to Wallerian degeneration, fibrosis and tissue adhesions that occur around and inside the nerve [15]. Autologous nerve grafting is the alternative solution of choice, but is related to scar formation, donor site morbidity, as well size and modality mismatch [16,17]. Research on biodegradable nerve conduits (NC) has gained increasing importance over the last 30 years [18], aiming to significantly improve the therapeutic outcome. A variety of materials and growth promoting agents is used, for the nerve to regrow inside the NC, but full functional recovery itself still remains an unmet challenge [19, 20].

It should be kept in mind, however, that the returning of function depends to some extent on the exact 3D microanatomy of the nerve, as well as the morphology of the conduit-nerve complex. This is where 2D histology, the gold standard of assessing anatomical recovery, is inherently challenged. We have thus proposed laboratory  $\mu$ CT as the ideal complement to histology, to achieve an effort-, time- and cost-effective 3D visualization of regenerating peripheral nerves with true isotropic resolution. The investigated specimens were provided by S. Madduri from the Center for Bioengineering and Regenerative Medicine (CBRM) of the University of Basel, who has also designed the animal experiments, together with D. F. Kalbermatten from the Department of Plastic, Reconstructive, Aesthetic and Hand Surgery (DPRAH) from the Basel University Hospital. L. Degruillier from the CBRM was involved in the animal interventions. From our group, G. Schulz provided help needed with the tomography measurements, P. Thalmann and S. E. Hieber were in charge of the data post-processing and analysis and B. Müller had an essential role in designing the tomographic study, as well as overlooking every step of the experiment, from data analysis to manuscript writing. The histological equipment needed for the specimen preparation was provided by S. Frank and J. Hench of the Neuropathology Department, University Hospital Basel. Customized sample holders were fabricated

by Sascha Martin and Stefan Gentsch of the Mechanics Shop, Physics Department of the University of Basel.

## 2 Results

### 2.1 Sensitivity comparison of absorption and grating-based phase tomography of paraffin-embedded human brain tissue



Highlights:

- Quantitative measurement of refractive index for medically-relevant specimen
- Comparison of representative absorption- and phase-contrast SR $\mu$ CT data
- Studying the effect of photon energy optimization for absorption measurements
- Absorption tomography proven as a time- cost- and effort-effective approach

# Sensitivity comparison of absorption and grating-based phase tomography of paraffin-embedded human brain tissue

Cite as: Appl. Phys. Lett. 114, 083702 (2019); <https://doi.org/10.1063/1.5085302>

Submitted: 11 December 2018 . Accepted: 12 February 2019 . Published Online: 28 February 2019

Christos Bikis , Griffin Rodgers , Hans Deyhle, Peter Thalmann, Alexander Hipp , Felix Beckmann , Timm Weitkamp , Stamatios Theocharis , Christoph Rau, Georg Schulz , and Bert Müller 



View Online



Export Citation



CrossMark

# Sensitivity comparison of absorption and grating-based phase tomography of paraffin-embedded human brain tissue

Cite as: Appl. Phys. Lett. 114, 083702 (2019); doi: [10.1063/1.5085302](https://doi.org/10.1063/1.5085302)

Submitted: 11 December 2018 · Accepted: 12 February 2019 ·

Published Online: 28 February 2019



Christos Bikis,<sup>1</sup> Griffin Rodgers,<sup>1,a)</sup> Hans Deyhle,<sup>1</sup> Peter Thalmann,<sup>1</sup> Alexander Hipp,<sup>2</sup> Felix Beckmann,<sup>2</sup> Timm Weitkamp,<sup>3</sup> Stamatios Theocharis,<sup>4</sup> Christoph Rau,<sup>5</sup> Georg Schulz,<sup>1</sup> and Bert Müller<sup>1</sup>

## AFFILIATIONS

<sup>1</sup>Biomaterials Science Center, University of Basel, 4123 Allschwil, Switzerland

<sup>2</sup>Institute of Materials Research, Helmholtz-Zentrum Geesthacht, 21502 Geesthacht, Germany

<sup>3</sup>Synchrotron Soleil, 91192 Gif-sur-Yvette, France

<sup>4</sup>National and Kapodistrian University of Athens, 11527 Athens, Greece

<sup>5</sup>Diamond Light Source Ltd., Didcot OX11 0DE, United Kingdom

<sup>a)</sup>Electronic mail: [griffin.rodgers@unibas.ch](mailto:griffin.rodgers@unibas.ch)

## ABSTRACT

Advances in high-resolution hard X-ray computed tomography have led to the field of virtual histology to complement histopathological analyses. Phase-contrast modalities have been favored because, for soft tissues, the real part of the refractive index is orders of magnitude greater than the imaginary part. Nevertheless, absorption-contrast measurements of paraffin-embedded tissues have provided exceptionally high contrast combined with a submicron resolution. In this work, we present a quantitative comparison of phase tomography using synchrotron radiation-based X-ray double grating interferometry and conventional synchrotron radiation-based computed tomography in the context of histopathologically relevant paraffin-embedded human brain tissue. We determine the complex refractive index and compare the contrast-to-noise ratio (CNR) of each modality, accounting for the spatial resolution and optimizing the photon energy for absorption tomography. We demonstrate that the CNR in the phase modality is 1.6 times higher than the photon-energy optimized and spatial resolution-matched absorption measurements. We predict, however, that a further optimized phase tomography will provide a CNR gain of 4. This study seeks to boost the discussion of the relative merits of phase and absorption modalities in the context of paraffin-embedded tissues for virtual histology, highlighting the importance of optimization procedures for the two complementary modes and the trade-off between spatial and density resolution, not to mention the disparity in data acquisition and processing.

© 2019 Author(s). All article content, except where otherwise noted, is licensed under a Creative Commons Attribution (CC BY) license (<http://creativecommons.org/licenses/by/4.0/>). <https://doi.org/10.1063/1.5085302>

Since the invention of the Bonse-Hart interferometer,<sup>1</sup> X-ray phase contrast imaging has been preferentially considered for light elements, i.e., the main constituents of human tissues, for which the decrement of the real part of the refractive index  $\delta$  is three orders of magnitude larger than the imaginary part  $\beta$  at photon energies on the order of 10 keV.<sup>2</sup> Therefore, researchers estimated that phase-contrast tomography could reach a hundred to thousand times greater sensitivity than absorption-contrast tomography.<sup>3,4</sup> Pioneering tomography studies with hard X-rays revealed that not only the widely used absorption-contrast and the newer phase-contrast imaging techniques provide complementary information but also phase imaging yields a substantially better contrast-to-noise ratio (CNR) than absorption. During the last two decades, high-resolution tomography in the

phase-contrast mode has enabled the visualization of individual cells<sup>5</sup> and even sub-cellular details<sup>6,7</sup> in the *post mortem* human brain. High-resolution X-ray phase-contrast tomography shows great promise for augmenting standard pathology in research and clinics with the so-called virtual histology.<sup>8–10</sup>

Several experimental results, however, indicate that conventional X-ray absorption tomography provides comparable CNR to phase tomography for paraffin-embedded soft tissues, i.e., those used in typical histopathological analysis. For example, conventional tomography of the paraffin-embedded brain<sup>11</sup> and peripheral nerves<sup>12</sup> has yielded sufficient CNR to identify biological cells and related microstructures. Thus, it is still unclear which method is more effective for the visualization of anatomical features in human tissues in the context of virtual histology.

Consequently, the aim of the present tomography study is a quantitative comparison of the density resolution of absorption- and phase-contrast modalities in the case of histopathologically relevant biological specimens embedded in paraffin. To this end, part of a formalin-fixed and paraffin-embedded human cerebellum was three-dimensionally visualized by means of conventional synchrotron radiation-based microcomputed tomography (SR $\mu$ CT) and double-grating interferometry (XDGI). For a complete comparison, SR $\mu$ CT data were also recorded at an optimized photon energy significantly lower for the chosen sample than the energy used for XDGI. The tomography datasets were rigidly registered, and the common volume was extracted to generate bivariate distributions to directly compare the CNR. Additionally, the absorption projections were filtered to compare the CNR of the modalities at an equal spatial resolution.

The human cerebellum specimen was selected with informed consent for scientific use. All the associated procedures were conducted in accordance with the Declaration of Helsinki and were approved by the ethics committee of the Medical School of the National and Kapodistrian University of Athens. The brain was extracted *post mortem* from a donated body and fixed in 4% histological-grade buffered paraformaldehyde. To allow for sufficient perfusion of solvents and liquid paraffin, 2-cm-thick cerebellum slices were produced, dehydrated in ascending ethanol solutions, transferred to xylene, and finally embedded in a paraffin/plastic polymer mixture, following the standard pathology procedure. Out of the obtained paraffin blocks, cylinders 6 mm in diameter were obtained by means of a stainless-steel punch.

The wavefront  $\psi$  immediately after passing through the specimen is given by projection approximation<sup>13</sup>

$$\psi(x, y, z) = \psi(x, y, 0) \exp \left[ -ik \int_0^z [\delta(x, y, z) - i\beta(x, y, z)] dz \right],$$

where  $k$  is the wavenumber and  $z$  the propagation direction. A detector placed near the sample measures the modulus squared of the wavefront, accessing the imaginary part of the index of refraction

$$I(x, y) = I_0(x, y) \exp \left[ -2k \int \beta(x, y, z) dz \right].$$

This expression is equivalent to Beer's law, with the linear attenuation coefficient  $\mu = 2k\beta$ . If a grating interferometer is placed behind the sample, the interference pattern fringes are shifted laterally by an angle  $\alpha_x$  given by the derivative of the wavefront phase shift

$$\alpha_x(x, y) = \frac{\partial \phi(x, y)}{\partial x} = \frac{\partial}{\partial x} \int \delta(x, y, z) dz.$$

Phase stepping allows for retrieval of  $\alpha_x$ , and reconstruction with a modified filter kernel allows for  $\delta$ -retrieval.<sup>14,15</sup>

Phase and absorption tomography measurements using a photon energy of 20 keV, denoted DPC 20 and ABS 20, were performed at the Diamond Manchester Imaging Beamline [I13-2, Diamond Light Source (DLS), UK]. Additionally, an absorption tomography measurement at a photon energy of 10 keV, denoted ABS 10, was performed at the P05 beamline (PETRA III, DESY, Hamburg, Germany), a facility operated by the Helmholtz-Zentrum Geesthacht.

This study comprises at least seven parameters. The impact of these parameters has been considered, allowing for a comparison of

the three dominant factors: (i) the contrast mechanisms, (ii) the selection of photon energy for absorption, and (iii) the balancing of the spatial resolution.

For a homogeneous specimen of diameter  $D$  with a linear attenuation coefficient  $\mu(E)$ , the optimal photon energy for an absorption measurement is found by setting  $\mu(E) \times D = 2$ .<sup>16</sup> For inhomogeneous specimens, a lower value is usually chosen. This value was 0.3 and 1.6 for ABS 20 and ABS 10, respectively, indicating that 10 keV is closer to the optimum efficiency criteria.

The XDGI setup consisted of a beam-splitting absorption grating and an equivalent analyzer grating with a periodicity of  $p_1 = p_2 = 7 \mu\text{m}$  and a gold structure height of  $70 \mu\text{m}$ . The ideal transmission of this interferometer is 25%. An inter-grating distance of 80 cm was used, corresponding to the first fractional Talbot order. Five phase step images were recorded per projection. The setup had a mean visibility of 35%.

Between DPC 20 and ABS 20, the gratings and the water bath (used to avoid phase wrapping) were removed, the exposure time reduced, and the detector distance set to 7 cm. This was the minimum distance without changing the rotation stage. For ABS 10, the specimen-detector distance was 1 cm to reduce edge enhancement. All projections were  $2 \times 2$  binned to improve the signal and ease data handling.<sup>17</sup> Table I lists the acquisition parameters.

The phase retrieval for DPC 20 was performed by applying a pixel-wise Fourier analysis.<sup>14</sup> The tomographic reconstruction relied on the standard filtered back-projection algorithm, which is implemented in Matlab (The MathWorks, Inc., Natick, USA), using a modified filter kernel (Hilbert transform).<sup>15</sup> Prior to reconstruction, Gaussian filters with  $\sigma = 1.52$  and  $\sigma = 1.48$  pixels were applied to the projections of ABS 20 and ABS 10, respectively. This filter size matched  $p_2$ , which is the lower resolution limit of the phase measurement.<sup>14</sup> The approximately equal spatial resolution was confirmed by

**TABLE I.** Acquisition parameters for the three measurements. Effective pixel sizes contain the magnification and binning.

	DPC 20	ABS 20	ABS 10
Facility	DLS	DLS	DESY
Photon energy	20 keV	20 keV	10 keV
Camera	pco.4000 <sup>a</sup>	pco.4000 <sup>a</sup>	KAF-09000 <sup>b</sup>
Array (binned)	2004 × 1336	2004 × 1336	1528 × 1528
Scintillator	LuAG	LuAG	CdWO <sub>4</sub>
	500 $\mu\text{m}$	500 $\mu\text{m}$	100 $\mu\text{m}$
Objective	PLAPON 2× <sup>c</sup>	PLAPON 2× <sup>c</sup>	POG 5× <sup>d</sup>
Numerical aperture	0.08	0.08	0.25
Effective pixel size	4.6 $\mu\text{m}$	4.6 $\mu\text{m}$	4.8 $\mu\text{m}$
Detector distance	80 cm	7 cm	1 cm
$t_{\text{exp}}$	5 × 5 s	2 s	1.5 s
# counts	5 × 2500	10 000	32 000
# projections	1201	1201	1201
Medium	Water	Air	Air

<sup>a</sup>PCO AG, Kelheim, Germany.

<sup>b</sup>EHD SciCam, EHD Imaging GmbH, Damme, Germany.

<sup>c</sup>Olympus Corporation, Tokyo, Japan.

<sup>d</sup>Präzisionsoptik Gera GmbH, Löbichau, Germany.

the selected line profiles, where the number of pixels defining the edges between paraffin and the molecular layer for the filtered absorption-contrast datasets was less than or equal to that for the phase-contrast dataset.

To obtain meaningful bivariate histograms, also known as joint histograms, the data have to be precisely registered. Therefore, an affine three-dimensional registration was performed by means of an algorithm to maximize mutual information,<sup>18–20</sup> with ABS 20 selected as a reference and DPC 20 or ABS 10 as the floating dataset. Tricubic interpolation was used for visualization, while the nearest neighbor interpolation was used for the analysis in order to avoid smoothing of the floating datasets.

Figure 1 shows a slice through the registered reconstructions of (a) DPC 20, (b) filtered and (c) unfiltered ABS 10, and (d) filtered and (e) unfiltered ABS 20. Related zoom-in views are given on the right to better visualize the (anatomical) features, i.e., the paraffin (PA), the molecular layer (ML), and the granular layer (GL). Purkinje cells can be identified between the ML and GL, see, e.g., bright dots in the zoomed view of (b). The white matter (WM) is found on the right side of each slice, with grayscale values between ML and GL.

Joint histograms from common volumes of tomography datasets allow for segmentation of specimen components<sup>21,22</sup> and direct comparison of the density resolution. Figure 2 shows the joint histograms of DPC 20 and filtered ABS 10 and filtered ABS 20. The histograms fit with a four-Gaussian model were chosen to match the number of features. The center and the width of the Gaussians are superimposed onto the joint histogram as a visual aid. The superior CNR of DPC 20 compared to the filtered ABS 20 is clear from the broadening of the Gaussian peaks. This is less evident for DPC 20 compared to ABS 10.

Equally sized regions of interest were selected within homogeneous areas characteristic of each (anatomical) feature in order to determine their index of refraction and the CNR. Paraffin was used as the reference material, as the surrounding medium was water for DPC 20 and air for ABS 20 and ABS 10. The measured  $\Delta\delta \pm \sigma_\delta$  (or  $\Delta\beta \pm \sigma_\beta$ ) values and the mean CNRs are shown in Table II. Both the histogram fits from Fig. 2 and the values from Table II indicate a nearly linear relationship between the real and imaginary parts of the refractive index, with  $\Delta\delta/\Delta\beta \approx 700$  at 20 keV.

We define the Relative Contrast Gain (RCG) as the ratio of the CNR of the phase dataset over various absorption datasets.<sup>23–25</sup> The filtered datasets have a similar spatial resolution, and therefore, the RCG indicates the image quality improvement of phase contrast compared to absorption contrast. The RCG depends not only on  $\Delta\delta/\Delta\beta$  but also on the sensitivity of the grating interferometer and on the tomographic reconstruction.

Table II shows the CNR and RCG for each dataset. Higher RCG values indicate a larger advantage of phase contrast over the dataset in question. Filtering increased the CNR by a factor of around 14 (5) for ABS 20 (ABS 10), underlining the importance of a comparison at an equal spatial resolution. The current study should initiate a detailed experimental study to understand the improvement of tomographic data quality by Gaussian filtering.

The absorption datasets, particularly ABS 20, where the sample-detector distance was larger, show edge enhancement, and thus, the phase retrieval proposed by Paganin *et al.* was applied.<sup>26</sup> Like Gaussian filtering, this reduces the noise at the expense of spatial resolution. The phase-retrieved 20 keV absorption dataset with  $\delta/\beta$  of 100,

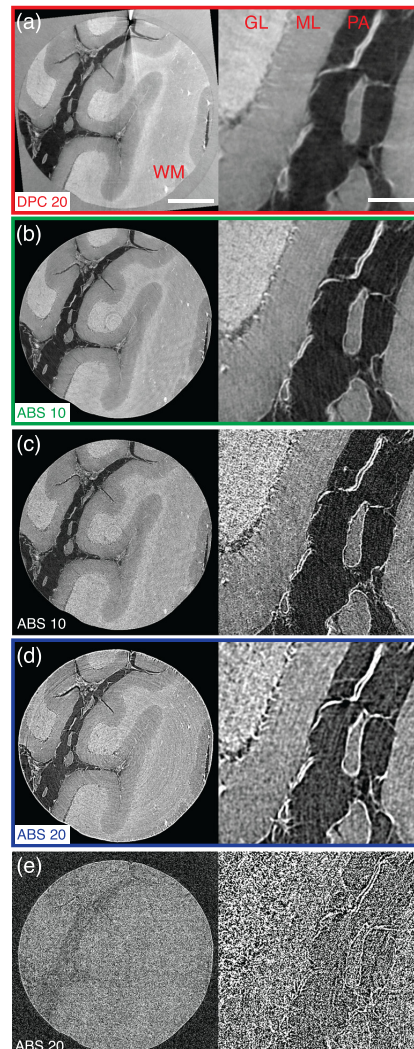


**FIG. 1.** One slice of the registered reconstructions of (a) DPC 20, (b) filtered ( $\sigma = 1.48$  pixels) and (c) unfiltered ABS 10, and (d) filtered ( $\sigma = 1.52$  pixels) and (e) unfiltered ABS 20. Features are indicated in (a): paraffin (PA), molecular layer (ML), granular layer (GL), and white matter (WM). Zoom-in views show a similar spatial resolution for (a)–(d). Gaussian filtering significantly improved CNR [(c) vs. (b) and (e) vs. (d)]. The scale bar in the slice (zoom) corresponds to 1.5 mm (150  $\mu\text{m}$ ). The gray scale corresponds to (a)  $\Delta\delta = [-1.1, 6.5] \times 10^{-8}$ , (b) and (c)  $\Delta\beta = [-1.4, 6.6] \times 10^{-10}$ , and (d) and (e)  $\Delta\beta = [-0.4, 1.1] \times 10^{-10}$ .

200, 500, and 1000 had CNR of 2.48, 4.16, 8.45, and 14.24, respectively. The spatial resolution of  $\delta/\beta$  of 200–500 matched the grating-based phase and filtered absorption datasets, based on the spectral power. Thus, in the context of the 20 keV measurement, Gaussian filtering

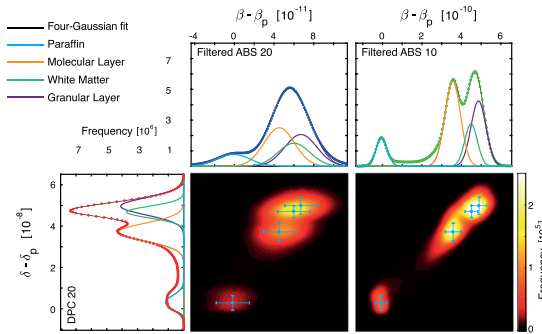


**FIG. 2.** Joint histograms of the filtered ABS 20 (middle) and filtered ABS 10 (right) with the DPC 20 dataset (y-axis). Individual histograms are also shown, which correspond to the projection of the joint histograms. Multi-Gaussian fits of the histograms are shown, with four Gaussians equal to the number of anatomical features. The centers and widths of these Gaussian fits are plotted on the joint histograms as a visual aid. The filtered ABS 20 has the lowest CNR, as evidenced by the broadest peaks. DPC 20 and the filtered ABS 10 show similar CNR. The peaks in the joint histograms indicate an approximately linear relationship between the real and complex parts of the refractive index throughout the specimen.

and Paganin's method produced similar image quality although the sample-detector distance was not optimized for Paganin's method.<sup>26</sup> The Gaussian filter was selected for this study because it requires no *a priori* knowledge of the refractive index and, unlike, e.g., binning, allows for fine control of the kernel size in order to match the spatial resolution between the datasets.

Photon energy optimization plays a large role in reducing the RCG (or increasing CNR) for the absorption measurements.  $\Delta\beta$  increased by a factor of over 7 by decreasing the photon energy from 20 keV to 10 keV, creating a larger difference in absorption, while still allowing sufficient transmission for counting statistics. Adjusting the photon energy greatly impacts the count rate due to the details of the insertion device, optics, and the detection system at each synchrotron facility. In our case, the count rate is more than tripled for the measurement at lower photon energy. Together, the higher count rate and the lower energy provided a CNR improvement of around 7 (2.5) for the unfiltered (filtered) datasets. Typically, photon energy is not optimized in XDGI measurements because gratings are designed for operation at a few specific energies.

For larger specimens, the criteria proposed by Grodzins suggest a higher optimal energy.<sup>16</sup> For example, an entire rat brain (assuming a

diameter of 12.5 mm) has an optimal photon energy of around 15 keV, while for a human brain (diameter 100 mm), it is around 50 keV. Therefore, it is not always the case that taking absorption at lower energies than the phase will improve the CNR. Nevertheless, most grating interferometers are designed for one specific energy, which may not be close to the optimal energy for absorption or phase measurements of a given specimen. The optimization of photon energy for grating-based phase contrast has not been experimentally studied. This study focuses on the case of 6 mm punches, a typical size for high resolution computed tomography experiments with effective pixel sizes in the micrometer range and fields-of-view of several millimeters.

The sensitivity of a grating interferometer can be described by the minimum resolvable deflection angle<sup>27</sup>

$$\alpha_{min} = \frac{p_2}{2\pi d} \frac{2}{V\sqrt{N}}.$$

Thus, the effect of increased counts can be extrapolated by the  $\sqrt{N}$  term, with the caveat that low count rates may lead to reduced visibility or a degraded spatial resolution due to mechanical instabilities over longer acquisition times. The relationship between the period of the second grating  $p_2$ , the inter-grating distance  $d$ , and the visibility  $V$  is more complex. The visibility depends on the transverse coherence length,  $l_c = \lambda L/s$  (photon wavelength  $\lambda$ , source-sample distance  $L$ , and source size  $s$ ),  $p_2$ , and the Talbot order  $n^{28}$

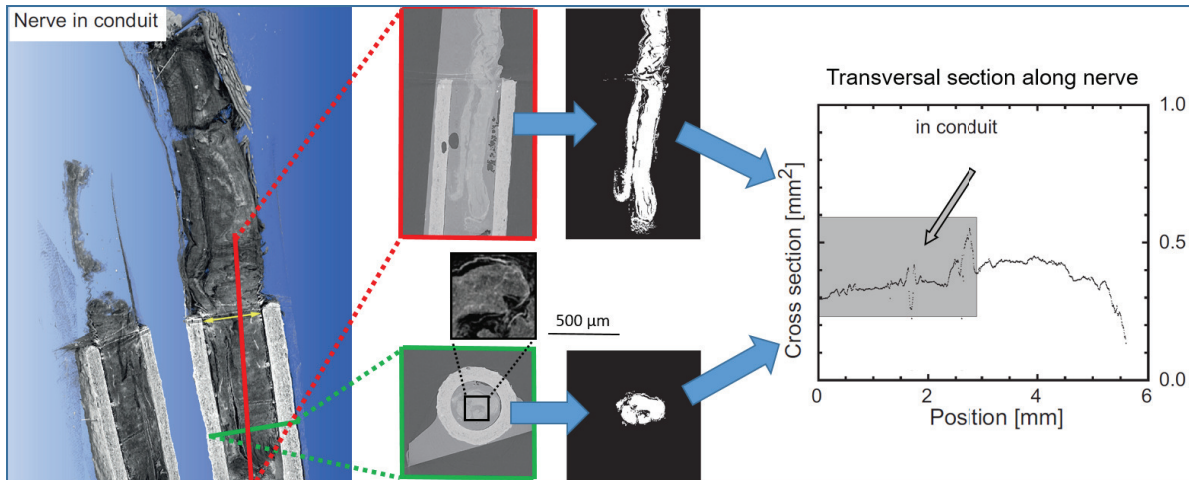
$$V = \exp [-(0.94np_2/l_c)^2].$$

This allows us to extrapolate to a grating interferometer with better-adapted parameters, e.g., a  $\pi$ -shifting first grating and a  $2.4 \mu\text{m}$  analyzer grating period with the visibility around 45% at the 11th Talbot order, corresponding to 485 mm for the 19 keV design energy (see Ref. 9). Compared to our setup, this would provide a sensitivity gain of  $\sqrt{2}$  from increased transmission, 2.9 from  $p_2$ , and 0.6 from  $d$ . The exact visibility cannot be calculated without knowing the coherence properties of the beamline, the motor stability, and the grating quality; however, our setup would be favored due to the smaller  $np_2$  (i.e., more robust against transverse incoherence). The spatial resolution is limited to at least twice  $p_2$ , and thus, the optimized setup would allow for CNR gain from filtering. We predict that an optimized grating interferometer could reasonably achieve four times greater sensitivity. This image quality improvement over absorption is still far less than the  $\Delta\delta/\Delta\beta$  ratio and should be weighed against the more complicated and time-consuming acquisition of XDGI.

**TABLE II.** Means and standard deviations of the measured index of refraction for each feature relative to paraffin. The values correspond to  $(\Delta\delta \pm \sigma_\delta) \times 10^{-8}$  for DPC 20,  $(\Delta\beta \pm \sigma_\beta) \times 10^{-11}$  for ABS 20, and  $(\Delta\beta \pm \sigma_\beta) \times 10^{-10}$  for ABS 10.

	CNR	RCG	Paraffin	Molecular layer	White matter	Granular layer
DPC 20	$17.2 \pm 2.7$	1.0	$0 \pm 0.22$	$3.62 \pm 0.26$	$4.51 \pm 0.23$	$5.06 \pm 0.38$
ABS 10 (filtered)	$10.6 \pm 1.2$	1.6	$0 \pm 0.33$	$4.03 \pm 0.40$	$4.80 \pm 0.49$	$5.13 \pm 0.71$
ABS 10 (unfiltered)	$2.2 \pm 0.2$	7.8	$0 \pm 1.54$	$3.89 \pm 1.94$	$4.63 \pm 2.23$	$4.96 \pm 3.13$
ABS 20 (filtered)	$4.2 \pm 0.3$	4.1	$0 \pm 1.34$	$5.47 \pm 1.42$	$6.29 \pm 1.63$	$7.27 \pm 1.85$
ABS 20 (unfiltered)	$0.3 \pm 0.02$	58.7	$0 \pm 18.97$	$5.46 \pm 21.02$	$6.31 \pm 22.04$	$7.26 \pm 28.60$

## 2.2 Three-dimensional and non-destructive characterization of nerves inside conduits using laboratory-based micro computed tomography



Highlights:

- 3D imaging of paraffin-embedded peripheral nerves without contrast agent achieved
- Micro-anatomical features of nerves resolved even inside conduit
- Automatic nerve segmentation despite characteristic artifacts
- Automatic extraction of anatomical parameters in a few minutes for a 100 mm<sup>3</sup> volume

## Three-dimensional and non-destructive characterization of nerves inside conduits using laboratory-based micro computed tomography

Christos Bikis<sup>a</sup>, Peter Thalmann<sup>a</sup>, Lucas Degruyillier<sup>b</sup>, Georg Schulz<sup>a</sup>, Bert Müller<sup>a,\*</sup>, Daniel F. Kalbermatten<sup>c</sup>, Srinivas Madduri<sup>b,\*\*</sup>, Simone E. Hieber<sup>a</sup>,

<sup>a</sup>Biomaterials Science Center, Department of Biomedical Engineering, University of Basel, CH.;

<sup>b</sup>Center for Bioengineering and Regenerative Medicine, Department of Biomedical Engineering, University of Basel, CH.;

<sup>c</sup>Department of Plastic, Reconstructive, Aesthetic and Hand Surgery, Basel University Hospital, CH.;

---

### Abstract

*Background.* Histological assessment of peripheral nerve regeneration in animals is tedious, time-consuming and challenging for three-dimensional analysis.

*New Method.* The present study reports on how and to what extent micro computed tomography of paraffin-embedded samples can provide a reliable three-dimensional approach for quantitative analysis of peripheral nerves.

*Results.* Rat sciatic nerves were harvested, formalin-fixed, positioned into nerve conduits (NC), paraffin-embedded, and imaged using a laboratory-based X-ray microtomography system with an isotropic voxel length of 4  $\mu\text{m}$ . Suitable quantitative measures were identified and automatically evaluated, i.e. nerve

---

\* Abbreviations: NC, nerve conduit;  $\mu\text{CT}$ , X-ray microtomography;

\* Corresponding author at: Biomaterials Science Center, Department of Biomedical Engineering, University of Basel, Gewerbestrasse 14, 4123, Allschwil, CH. Tel.: +41 (0)61 207 5430, Fax: +41 (0)61 207 54 99

\*\* Corresponding author at: Center for Bioengineering and Regenerative Medicine, Department of Biomedical Engineering, University Hospital Basel, Spitalstrasse 21/Petersgraben 4, 4031, Basel, CH. Tel.: +41 (0)61 556 5049, Fax: +41 (0)61 265 25 25

Corresponding author at: Biomaterials Science Center, Department of Biomedical Engineering, University of Basel, Gewerbestrasse 14, 4123, Allschwil, CH. Tel.: +41 (0)61 207 5433, Fax: +41 (0)61 207 54 99

Email addresses: bert.mueller@unibas.ch (Bert Müller), srinivas.madduri@unibas.ch (Srinivas Madduri), simone.hieber@unibas.ch (Simone E. Hieber)

length, cross-sectional area and volume, as well as vascular structures, to be used as an assessment and comparison indicator of regeneration quality.

*Comparison with Existing Methods.* Compared to imaging using contrast agents, the investigated specimens can subsequently undergo the conventional histological analysis without requiring additional preparation steps. Contrast and spatial resolution are also increased significantly.

*Conclusions.* We demonstrate the potential of the micro computed tomography for non-destructive monitoring of peripheral nerves inside the conduits.

*Keywords:*  $\mu$ CT, X-ray, 3D imaging, computed tomography, nerve segmentation, vessel assessment

---

## 1. Introduction

Histology and histopathology focus on the study of cellular and tissue microanatomy in health and disease, respectively. They play a prominent role, both in research and clinical practice and are based on the main principle of examining tissue slices under an optical microscope. In several applications, however, this approach is not straightforward. In-vivo imaging methods for monitoring axon growth using fluorescence lack micrometer resolution and offer a maximal penetration depth close to 2 mm (Kerschensteiner et al., 2005). Immunohistochemical staining is the gold standard for the analysis of regenerated nerve tissue, but exhaustive serial sectioning is demanding for the evaluation in three dimensions (Godinho et al., 2013; Madduri et al., 2010b). Electron micrographs offer a high degree of lateral resolution, but the approach is associated with sample size constraints (Godinho et al., 2013).

It is known that X-ray microtomography ( $\mu$ CT) of soft tissues and nerves scanned in aqueous solutions provides images with limited contrast, due to the weak difference of tissue constituents in X-ray absorption. Therefore, iodine as contrast agent, has been applied for the X-ray imaging of nerves in conduits

(Hopkins et al., 2015). Very recently it has been demonstrated that paraffin embedding of human cerebellum allows for the visualization of individual  
20 Purkinje cells without staining, using a laboratory  $\mu$ CT system (Khimchenko et al., 2016) and their segmentation using feature-based filtering of synchrotron radiation  $\mu$ CT data (Hieber et al., 2016). We hereby assume such a label-free approach is also suitable for peripheral nerves, that have a great demand for high-throughput regeneration monitoring. Hence, we propose to employ a  
25 multi-step procedure combining tissue preparation, laboratory micro computed tomography and tailored image analysis to quantitatively characterize regenerating nerves inside an absorbable nerve conduit (NC) in a true three-dimensional manner. This non-destructive method will be applied before the preparation of histological sections, also aiding in the selection of the appropriate cutting planes  
30 (Stalder et al., 2014). For this feasibility study, healthy rat sciatic nerves were explanted and embedded in paraffin inside and outside a collagen NC (Madduri et al., 2010a).

In order to exhaust the full capacity of micro computed tomography (Holme et al., 2014), excess paraffin was removed as required, by means of applying a  
35 specific preparation protocol. Tomography data were acquired with high contrast and analyzed by a software developed for both rat nerves with and without NC. Identical anatomical details were identified in both cases. Additionally, the volume, area and length of the investigated nerves and their vasculature were also calculated in an automated approach, allowing for high-throughput investigations of nerve regeneration.  
40

## 2. Materials and Methods

The study was conducted in compliance with the ethical instructions of the Veterinary Office of the Kanton of Basel-Stadt (Basel, Switzerland), permission number 25212. Three sciatic nerves were surgically extracted from healthy  
45 Sprague Dawley rats. Collagen NCs were fabricated by spinning mandrel technology, as illustrated previously (Madduri et al., 2010a). Insoluble collagen

(2.5%, w/w) was swollen in 1 M acetic acid and homogenized with a high-speed mixer at 10,000 rpm (Polytron®, Kinematica, Lucerne, Switzerland) for 1 minute. The homogeneous collagen dispersion was applied via a syringe onto 50 a spinning Au-coated mandrel (diameter of 1.5 mm), installed in a sideways reciprocating apparatus, and the solvent was dried off under laminar airflow. The resulting tubes were neutralized by incubation in 0.1 M di-sodium hydrogen phosphate (pH of 7.4) for 1 h. The tubes were finally cut into 14 mm long specimens, which were cross-linked by physical means, i.e. by subjecting the 55 collagen tubes to a dehydro-thermal treatment (DHT) at a temperature of 110 °C and a pressure of 20 mbar for 5 days. The resulting tubes exhibited an outer diameter of 2.5 mm and inner diameter of 1.5 mm.

The nerves were fixed in formalin solution and subsequently embedded in paraffin blocks according to standard histological preparation. In order to optimize 60 the specimen's diameter for the tomography and to avoid entrapped air bubbles the paraffin embedding procedure was optimized. The long nerve was cut in two parts for ease of placing the nerve segments inside the conduit and further to avoid any tissue deformation over the course of tissue alignment along the lumen of the NC. After inserting the two segments of nerve, each from the 65 opposite opening of NC, the NC-nerve complex was embedded in paraffin.

The  $\mu$ CT system used for this study was the nanotom®m (phoenix |x-ray, GE Sensing & Inspection Technologies GmbH, Wunstorf, Germany). It is equipped with a 180 kV nanofocus transmission source and a  $3072 \times 2400$  pixels GE DXR detector. For all the presented measurements, the acceleration voltage 70 was set to 60 kV and the beam current to  $280 \mu\text{A}$ . Source-to-specimen and source-to-detector distances were 9 mm and 225 mm, respectively, resulting in an effective pixel size of  $4 \mu\text{m}$ . For all specimens, 1800 projections were acquired equiangularly over the range of  $360^\circ$ . In order to increase photon statistics, nine 75 images with an exposure time of 0.5 s each were averaged at each angular position. This resulted in a total scanning time of 150 minutes for one height step covering a nerve section 9.6 mm long. For specimens longer than 9.6 mm, two or more height steps were acquired and stitched after reconstruction (Müller

et al., 2012).

To reduce the effect of faulty detector pixels appearing constantly dark or  
80 bright in the projections, the acquired radiographs were filtered with a 2D me-  
dian filter with a  $3 \times 3$  kernel using the open-source software ImageJ (Schnei-  
der et al., 2012), prior to reconstruction. Thereby the contrast considerably  
increased, as found in the related absorption histograms, at the expense of  
negligible blurring. The filtered radiographs were reconstructed using the nan-  
85 otom®m manufacturer's software phoenix datosx 2.0.1 - RTM (GE Sensing &  
Inspection Technologies GmbH, Wunstorf, Germany), which employs a mod-  
ified Feldkamp cone beam reconstruction algorithm. Subsequently, the three-  
dimensional datasets were imported in the VGStudio MAX 2.1 (Volume Graph-  
ics GmbH, Heidelberg, Germany) software and scaled to the same gray-scale  
90 range necessary for image analysis. These 16-bit data sets have a size of ap-  
proximately 2 GB considering 1 cm of nerve. The VGStudio MAX was used for  
the three-dimensional rendering of the acquired tomograms.

For the morphological analysis, the paraffin-embedded nervous tissue, partly  
within the conduit, has to be segmented. Related steps of this procedure are  
95 illustrated in Figure 1. Image (a) represents the raw data. Image (b) shows  
that the contrast in the raw data was sufficient to successfully apply the Otsu  
method (Otsu, 1979), in order to digitally remove the scaffold. A distance trans-  
form served for removing a thin part (3-6 voxels) of the remaining specimen's  
surface, which was followed by selecting the largest connected component (c).  
100 This step was particularly needed to separate the specimen from heavy streak-  
ing and artifacts caused by the remaining air bubbles. As the artifacts were  
removed from the histograms, a second thresholding step using Otsu's method  
was applied (d). Given that the Gaussian distributions of the bare paraffin  
and the paraffin-embedded specimen in the absorption histograms were insuffi-  
105 ciently separated, this second thresholding step did not result in perfect virtual  
paraffin removal and created some voids inside the tissue. Such kind of noise  
was removed using a 2D median filter with a kernel of size  $3 \times 3$  (e). The  
segmentation was finalized by selecting the largest connected component and

applying an adaptive void-filling filter (f). After segmentation, the nerve was  
110 skeletonized by calculating the geometrical center for each slice. The entire seg-  
mentation and analysis procedure was performed in Matlab (MATLAB 2016a,  
The MathWorks, Inc., Natick, Massachusetts, United States).

Since the X-ray absorption values of the vessels overlap with the ones of  
other structures, a feature-based segmentation is applied to segment them. The  
115 probability of a voxel to belong to a vessel is determined by the established  
Frangi-Filter that examines the eigenvalues of the Hessian matrix (Frangi et al.,  
1998). The filter parameters were chosen to  $\alpha = 0.1$ ,  $\beta = 0.1$ ,  $\gamma = 0.2$  in the  
Matlab implementation by Kroon (2009). The voxel range was between one and  
three and the threshold of vesselness 0.4 for the normalized dataset.

120 **3. Results**

*3.1. Descriptive evaluation*

Figure 2 compares representative slices of two CT datasets showing the  
same nerve. In the presented cross sections one can readily recognize the mi-  
croanatomy of the selected nerve. In particular, the components including the  
125 epineurium and perineurium membranes surrounding the main axonal mass can  
be identified. The characteristic microanatomy of the nerve fascicle bundles is  
also visible. At some positions, the vasa nervorum (white-colored arrowheads)  
inside the nerve bulk exhibit a considerably higher X-ray absorption than their  
surrounding nervous tissue.

130 The left section also contains the porous conduit, which can be quantitatively  
characterized as well. Both the surface morphology as well as the locations and  
sizes of the individual pores inside the scaffold material are accessible.

In general, the nerve visualization inside the conduit is challenging because of  
its relatively high X-ray absorption. Artefacts such as streaks impede a detailed  
135 description. The images demonstrate, however, that the present experimental  
setup enables us to obtain results without significant differences between the  
bare nerve and the nerve within the conduit. The remaining differences are

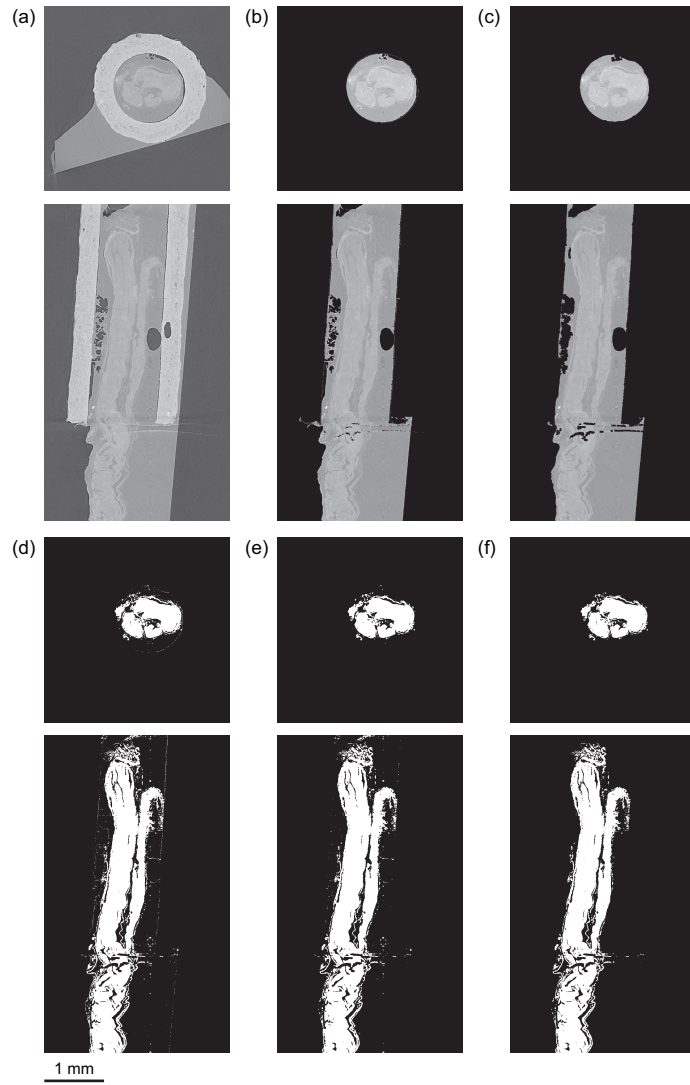


Figure 1: A cross-sectional and a longitudinal section of a selected dataset before and after segmentation: (a) original (b) air and scaffold virtually removed (c) boundary eroded and largest object selected (d) paraffin virtually removed and dataset binarized (e) median filtered and (f) largest object selected and voids filled.

limited deformations, a result of nerve handling between the acquisitions of the tomograms. Streak artifacts are rare.

140 Contrary to histology, tomography not only allows two-dimensional imaging in predefined directions but also the three-dimensional rendering with isotropic voxel size. Figure 3 shows an exemplary rendering, where a selected specimen is virtually cut into two parts along the symmetry axis. The internal structure of the two rat sciatic nerve segments, the gap between them, as well as the 145 surrounding conduit can be simultaneously visualized.

### 3.2. Nerve Segmentation

The quantification of nerve regeneration requires the identification of the nervous tissue within the three-dimensional dataset. The contrast, density resolution, of the CT data enables a clear distinction between the air, the paraffin, 150 the scaffold, and the nervous tissue based on their specific X-ray attenuation. Thus, a thresholding approach (Müller et al., 2002) performs well for the segmentation as illustrated in Figure 1, cp. especially images (b) and (d). Imaging artifacts at the surface and noise due to photon statistics can be handled appropriately by filtering techniques see images (c), (e) and (f). As a result, the 155 segmentation mask in Figure 1 (f) matches well with the nervous tissue shown in the non-treated data set (Figure 1 (a)). Even thin layers of nervous tissue including the epineurium and perineurium membranes are represented clearly.

### 3.3. Nerve characterization by geometrical parameters

The contrast in the tomography data was sufficient to automatically segment 160 the nerve. The success of the procedure was manually validated. For this purpose, two experts compared the original and related segmented data section-wise.

In a subsequent step, the segmented nerve was charted to extract the morphological data, i.e. volume, length, and cross section. Table 1 lists these 165 geometrical parameters for the three selected nerves.

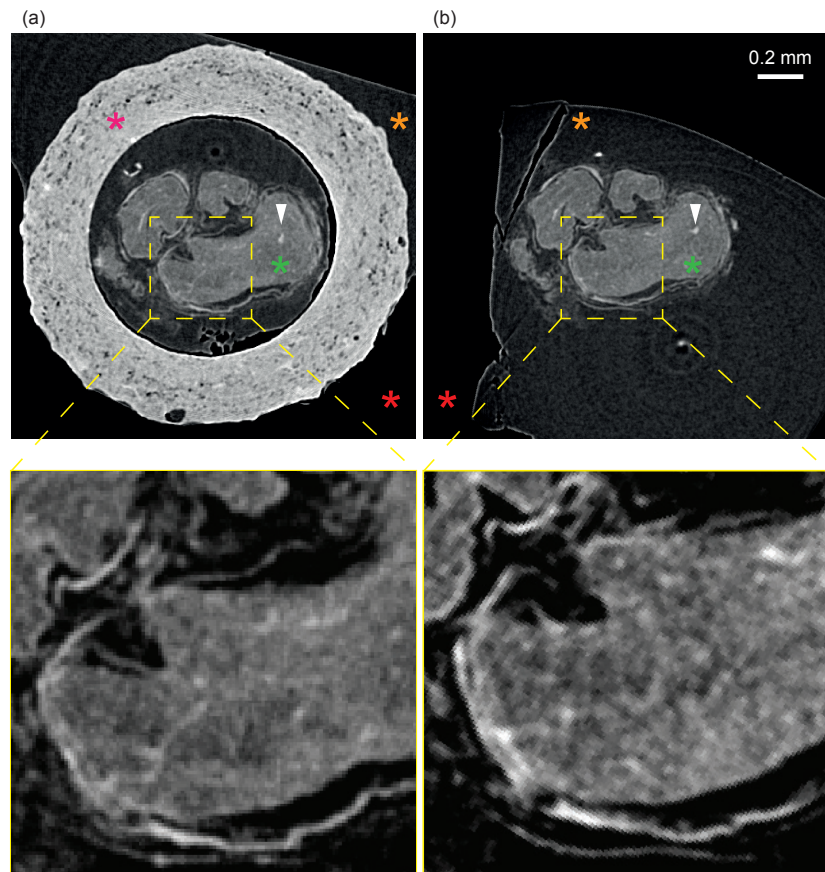


Figure 2: (a) A cross-sectional view of a rat sciatic nerve (green-colored asterisk) inside the collagen scaffold (magenta-colored asterisk). The nerve-scaffold complex is embedded in paraffin (orange-colored asterisk). The lowest absorbing element in the picture is the air (red-colored asterisk). (b) Related section of the same nerve subsequently scanned without the conduit. Higher X-ray absorption values are represented by lighter gray shades.

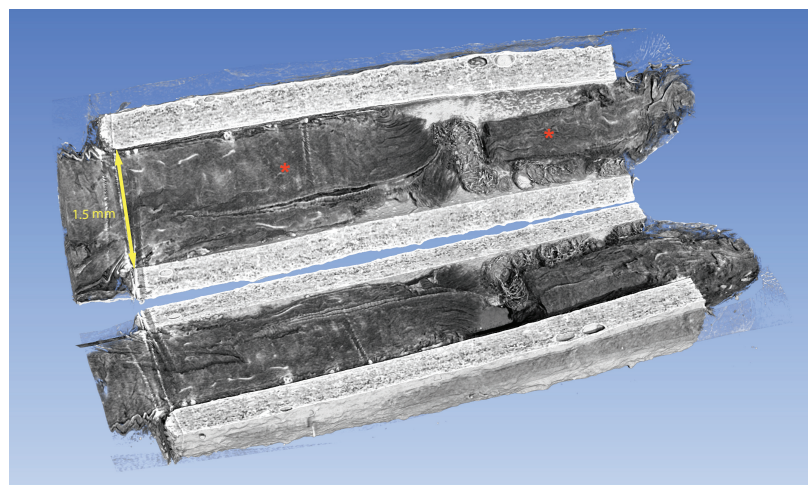


Figure 3: A three-dimensional view of a selected nerve specimen comprised of two parts (red-colored asterisks) inside a collagen scaffold. The specimen was digitally sectioned, and the paraffin was made transparent. The two components visible are the rat sciatic nerve tissue (gray) and the collagen scaffold (white). The NC has a length of 14 mm and an inner diameter of 1.5mm.

Table 1: Measured geometrical parameters of three selected nerves

Sample number	Volume (mm <sup>3</sup> )	Length (mm)	Average cross section (mm <sup>2</sup> )
1	3.54 ± 0.39	9.59 ± 0.23	0.45 ± 0.05
2	1.81 ± 0.20	11.00 ± 0.28	0.34 ± 0.04
3	2.81 ± 0.31	11.92 ± 0.38	0.47 ± 0.05

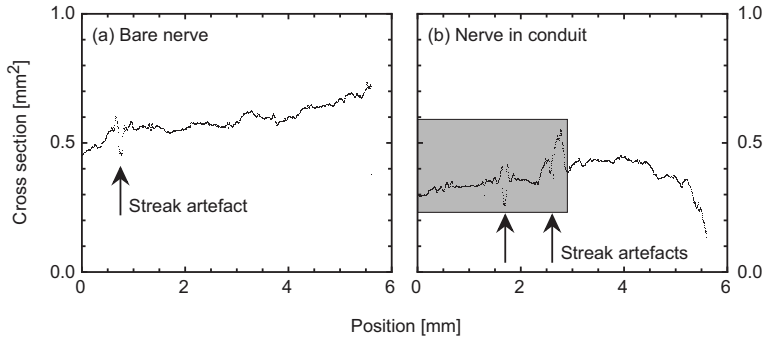


Figure 4: The cross-sectional area along the longitudinal direction of the specimen; (a) bare nerve and (b) nerve inside the conduit. Discontinuities as indicated by the arrows relate to streak artifacts and are more frequently found at the NC.

Although  $\mu$ CT provides true micrometer resolution, the error bars are rather large. Inaccuracy is caused by discontinuities in the curve progression, as indicated in Figure 4. These discontinuities are caused by streak artifacts, due to high X-ray absorbing species. Therefore, the streaks are more frequently found at conduits and their interfaces (Fig. 4).

From the anatomical point of view, the cross-sectional area should be consistent from section to section. Therefore, the smoothness of the curves in the diagrams of Figure 4 is an indicator for the reasonable performance of the automatic segmentation.

#### 175 3.4. Vessel visualization

Figure 5 shows the segmented vessels after filtering the three-dimensional data set for tubular structures. At some positions the segments are apparently connected to streak artifacts, which impedes their segmentation. In general, one

recognizes the course of the vessels, although they are frequently interrupted  
<sup>180</sup> within the acquired three-dimensional data. The related virtual sections prove  
the significantly higher X-ray absorption of the segmented parts of the visualized  
blood vessel system.

#### 4. Discussion

The microanatomy of rat peripheral nerves has been studied in detail, see  
<sup>185</sup> e.g. Bertelli et al. (1995). The quality of the present CT slices is almost comparable to the slides of digitized histology with medial magnification. Previous imaging data were mainly obtained optically and restricted in two dimensions showing the nerve's surface or selected cross sections, or the third direction of the data set was hardly resolved better than  $50\text{ }\mu\text{m}$ . The performance of imaging techniques including micro computed tomography can be characterized by  
<sup>190</sup> the spatial and density resolution (Thurner et al., 2004). Whereas the accessible spatial resolution only depends on the experimental setup and the components included, the density resolution (contrast) crucially depends on the specimen preparation, i.e. dehydration, embedding, and staining. CT-systems for animal experiments with a rotating gantry, as used by Hopkins et al. (2015) are usually  
<sup>195</sup> not stable enough to reach a spatial resolution below  $20\mu\text{m}$ . Using advanced micro computed tomography systems based on nanofocus X-ray tubes, such as nanotom<sup>®</sup>m, one can achieve a spatial resolution below  $1\text{ }\mu\text{m}$ . The effective spatial resolution, however, also depends on the maximal diameter of the specimen and the detector pixels (Holme et al., 2014). Therefore, the effective pixel size in the present study was restricted to  $2\mu\text{m}$  based on the specimens' dimensions. In order to improve acquisition time and image quality and to avoid sample deformation as a result of thermal irradiation from the X-ray source, the  
<sup>200</sup> magnification was set to  $25\times$ , i.e., an effective pixel size of  $4\mu\text{m}$ . The spatial resolution was estimated close to  $6\mu\text{m}$  (Bikis et al., manuscript 2). This result is an improvement of an order of magnitude with respect to the study of Hopkins et al. (2015) in each of the three orthogonal directions.

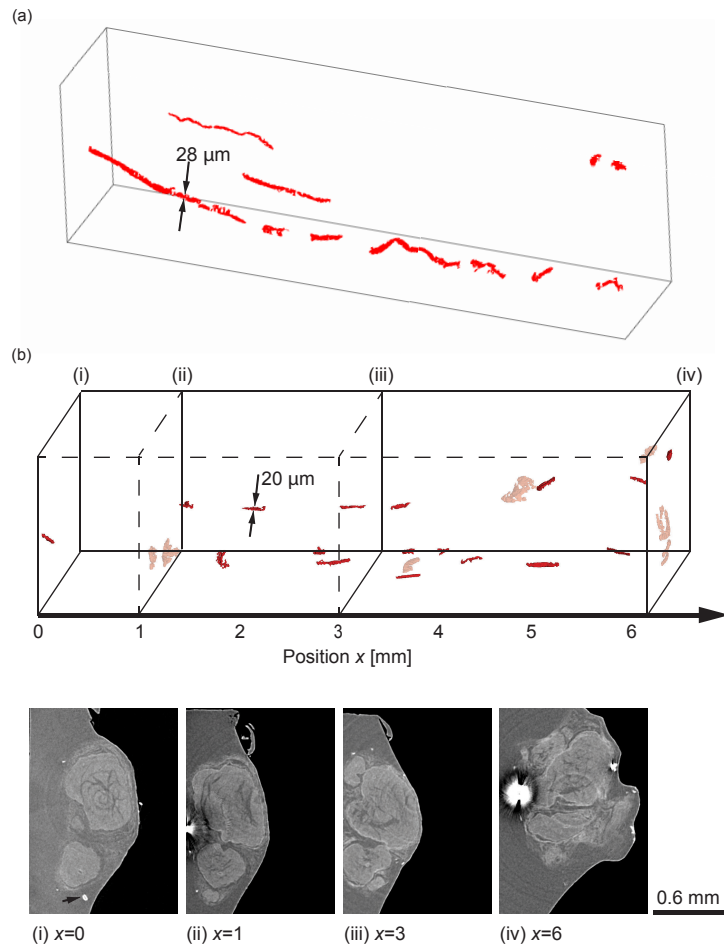


Figure 5: The three-dimensional images (a) and (b) elucidate that the vessel tree is only partly revealed through a series of segments. The largest connected component in (a) has a volume of  $1.9 \times 10^5 \mu\text{m}^3$  and an estimated mean diameter and length of 28 and 311  $\mu\text{m}$  respectively. The four selected virtual sections (i-iv), assigned to the position within the three-dimensional representation of the segmented data (b), show that the vessel segments are characterized by high X-ray absorbing species given in white, as indicated for example by the arrow in (i). The streak artifacts, also appearing white in the virtual sections, can lead to false segmentation and were digitally made semi-transparent in the three-dimensional representation.

It should be noted that paraffin embedding has advantages with respect to employing contrast-enhancing species such as Lugol's iodine. The employment  
<sup>210</sup> of highly X-ray-absorbing species necessitates higher accelerating voltages and generally impairs the image quality.

The contrast of the  $\mu$ CT data collected within the current study is surprisingly high, as soft-tissue components generally exhibit much less contrast than bony tissues. This is the result of local density and composition distributions.  
<sup>215</sup> Here, the embedding of the nerve into paraffin, a mixture of hydrocarbons with a density of about  $0.9 \text{ g/cm}^3$ , is advantageous compared to the use of fixation fluid with a density of  $1.0 \text{ g/cm}^3$ . It is, however, important to avoid confined bubbles, which give rise to severe artifacts. Therefore, several trials to improve the paraffin embedding were tested, before a reasonable result could be found.

<sup>220</sup> An important achievement of the present study is the nerve visualization inside the NC, which is a major challenge, since the NC material exhibits significantly higher X-ray absorption than the nerve tissue. The obtained  $\mu$ CT data, however, prove that both the microanatomy of the nerve inside the conduit and the porous structure of the scaffold are accessible in a reasonable manner.

<sup>225</sup> Given that  $\mu$ CT is a non-destructive technique, conventional histology can be performed subsequently. In addition, contrarily to imaging approaches based on contrast agents, that require additional, time-consuming tissue processing steps, the presented approach requires hardly any adaptation of the standard histological paraffin-embedding protocol. Even in the best case scenario, where  
<sup>230</sup> the iodine contrast agent can be removed without affecting histology, staining and de-staining the samples prior to and after imaging, respectively, needs at least four additional days of time. This time delay can be considerably increased, since incubation times are increasing with sample dimensions (Hopkins et al., 2015). Here, the  $\mu$ CT data can readily support the appropriate selection of  
<sup>235</sup> the direction of the histological sections virtually cutting the tomography data (Stalder et al., 2014) and saving precious time. Anatomical landmarks guide the orientation and allow for the precise choice of the desired plane of interest.

A three-dimensional dataset with minimized artifacts is a prerequisite for

the successful application of segmentation tools. Currently the segmentation is  
240 often carried out manually, which is time-consuming and error-prone due to the thousands of sections and the large size of data at the order of several gigabytes. Therefore, an increasing number of research teams employ computer software for segmentation and analysis tasks, see e.g., Long et al. (2014); Irshad et al. (2014). The automatic procedure proposed in the present work is sufficiently  
245 accurate to extract geometrical characteristics of the nerve microanatomy even inside the higher X-ray absorbing conduit.

To underline the reliability of the segmentation, four selected sections were segmented manually and compared to the corresponding automatic result. The manual segmentation included the nervous and connective tissues and was based  
250 on visual inspection. Inclusions of the nervous tissue were considered in the manual segmentation only if thicker than  $50 \mu\text{m}$ . The voxel segmentation resulted in 6% false positive and 17% false negative. The segmented area in the cross section shows an error of 11%. Thus, we assume an error of 11% in the volume measurement, as well.

255 The length of the computed centerline can be affected by the uncertainty of the cross section segmentation and the related error bars are given in Table 1. The minimal length was determined after smoothing with a moving average filter with a kernel size of 10 voxels and the maximal length was determined without smoothing.

260 It is well known, that a higher electron beam current within the source gives rise to a higher photon flux allowing for a shorter acquisition time due to increased photon statistics, see e.g. Holme et al. (2014). Therefore, one tries to work nearly the maximally possible beam current. Reducing the electron beam current, however, one not only extends the lifetime of the filament, but  
265 also obtains higher spatial resolution because of the smaller cross-over (beam spot). The choice of the beam current is, therefore, an optimization task. For our study, we have found that 90% of the maximally possible beam current guarantees the necessary spatial resolution and photon statistics (contrast) at reasonable acquisition time. The acquisition time can be considerably shortened

270 by means of a liquid jet anode (Bartels et al., 2013). Such an experimental setup also allows phase X-ray imaging, beneficial for the three-dimensional nerve visualization with increased contrast.

275 Nonetheless, the observed streak artifacts increase the error bars to about 15%, a value to be further optimized. Given that we have already optimized the selection of the appropriate scanning parameters, sample preparation itself needs to be further improved towards that goal. Avoiding high-absorbing species and cracks that can be present in the paraffin block, as well as trapped air bubbles, mainly on the nerve surface, will greatly reduce the presence of streak artifacts. Further efforts for refining our established procedure are under progress.

280 The vascular network is an essential component of healthy tissue, therefore the consideration of vessels in nerves is an important aspect of their evaluation. In this study, the feature-based filter for blood vessels was set up to detect tubular microstructures with a diameter starting from  $8 \mu\text{m}$ , which corresponds to two voxel lengths. The application of the filter enabled us to detect blood 285 vessels with a diameter larger than  $12 \mu\text{m}$ . Nevertheless, the blood vessels of the formalin-fixated and paraffin-embedded tissue tend to collapse and are, therefore, less appropriate to estimate the spatial resolution reached within the present study. The vessel tree is only partly visible. Probably, only the remaining blood clots were made visible, which show relatively high X-ray absorption 290 because of the iron present. These datasets already provide a reasonable estimate of the vessel density.

## 5. Conclusions

295 Advanced conventional  $\mu\text{CT}$  allows the three-dimensional characterization of paraffin-embedded nerves even inside a conduit of significantly higher X-ray absorption than the tissue. In spite of occurring streak artifacts, our approach employs fully automatic tools that yield reliable results. Consequently, reproducible non-destructive evaluations of specimen series have become possible in quantitative manner within hours (ref. publication 2). The method is fully

compatible with established histology to be performed subsequent to the tomography measurements.  
300

## 6. Acknowledgments

The authors thank Stephan Frank and Jürgen Hench from the Neuropathology Department, Basel University Hospital, for allowing the use of histological equipment, as well as Sascha Martin and Stefan Gentsch from the Mechanics Shop, Physics Department, University of Basel for providing the sample holders.  
305  
The project was supported by SNSF projects 144535 and 133802.

## 7. Conflicts of interest

The authors declare no conflict of interest

## References

- 310 Bartels, M., Hernandez, V.H., Krenkel, M., Moser, T., Salditt, T., 2013. Phase contrast tomography of the mouse cochlea at micro-focus x-ray sources. Applied Physics Letters 103, 083703. URL: <https://doi.org/10.1063/1.4818737>, doi:10.1063/1.4818737, arXiv:<https://doi.org/10.1063/1.4818737>.
- 315 Bertelli, J.A., Taleb, M., Saadi, A., Mira, J.C., Pecot-Dechavassine, M., 1995. The rat brachial plexus and its terminal branches: an experimental model for the study of peripheral nerve regeneration. Microsurgery 16, 77–85.
- Frangi, A.F., Niessen, W.J., Vincken, K.L., Viergever, M.A., 1998. Multiscale vessel enhancement filtering. Springer Berlin Heidelberg, Berlin, Heidelberg.  
320 pp. 130–137. URL: <http://dx.doi.org/10.1007/BFb0056195>, doi:10.1007/BFb0056195.
- Godinho, M.J., Teh, L., Pollett, M.A., Goodman, D., Hodgetts, S.I., Sweetman, I., Walters, M., Verhaagen, J., Plant, G.W., Harvey, A.R., 2013. Immuno-histochemical, ultrastructural and functional analysis of axonal regeneration

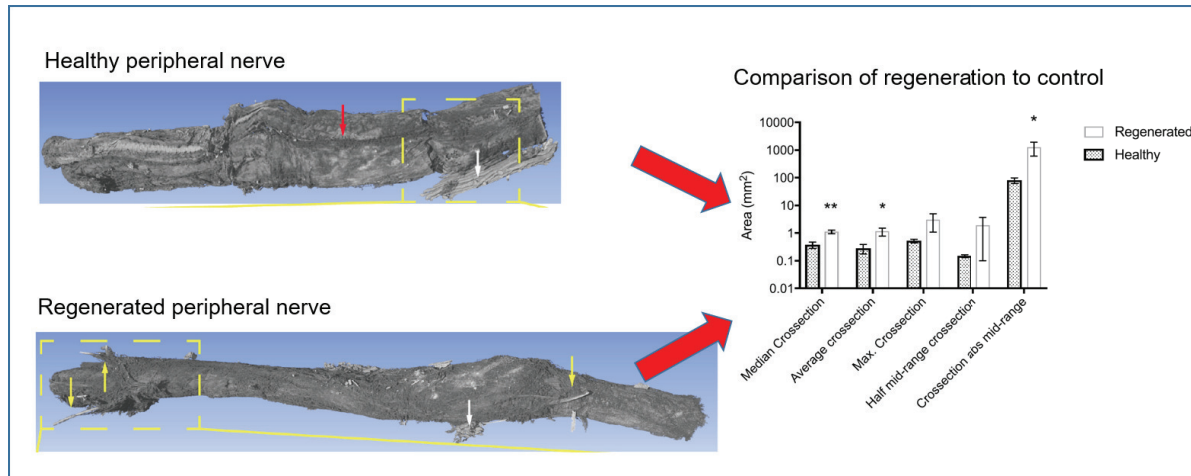
- 325 through peripheral nerve grafts containing schwann cells expressing BDNF,  
CNTF or NT3. PLoS One 8, e69987. URL: <http://dx.doi.org/10.1371%2Fjournal.pone.0069987>, doi:10.1371/journal.pone.0069987.
- Hieber, S.E., Bikis, C., Khimchenko, A., Schweighauser, G., Hench, J.,  
Chicherova, N., Schulz, G., Müller, B., 2016. Tomographic brain imaging with  
330 nucleolar detail and automatic cell counting. Scientific Reports 6, 32156.
- Holme, M.N., Schulz, G., Deyhle, H., Weitkamp, T., Beckmann, F., Lobrinus,  
J.A., Rikhtegar, F., Kurtcuoglu, V., Zanette, I., Saxer, T., Müller, B.,  
2014. Complementary x-ray tomography techniques for histology-validated  
3d imaging of soft and hard tissues using plaque-containing blood vessels as  
335 examples. Nature Protocols 9, 1401–1415. URL: <http://dx.doi.org/10.1038/nprot.2014.091>.
- Hopkins, T.M., Heilman, A.M., Liggett, J.A., LaSance, K., Little, K.J., Hom,  
D.B., Minteer, D.M., Marra, K.G., Pixley, S.K., 2015. Combining micro-  
340 computed tomography with histology to analyze biomedical implants for pe-  
ripheral nerve repair. Journal of Neuroscience Methods 255, 122–30.
- Irshad, H., Veillard, A., Roux, L., Racocceanu, D., 2014. Methods for nuclei  
detection, segmentation, and classification in digital histopathology: a review-  
current status and future potential. IEEE reviews in biomedical engineering  
7, 97–114.
- 345 Kerschensteiner, M., Schwab, M.E., Lichtman, J.W., Misgeld, T., 2005. In vivo  
imaging of axonal degeneration and regeneration in the injured spinal cord.  
Nature Medicine 11, 572–7.
- Khimchenko, A., Deyhle, H., Schulz, G., Schweighauser, G., Hench, J.,  
Chicherova, N., Bikis, C., Hieber, S.E., Müller, B., 2016. Extending two-  
350 dimensional histology into the third dimension through conventional micro  
computed tomography. NeuroImage 139, 26–36.

- Kroon, D.J., 2009. Hessian based frangi vesselness filter. <http://www.mathworks.com/matlabcentral/fileexchange/24409-hessian-based-frangi-vesselness-filter>.
- <sup>355</sup> Long, H.Q., Xie, W.H., Chen, W.L., Xie, W.L., Xu, J.H., Hu, Y., 2014. Value of micro-ct for monitoring spinal microvascular changes after chronic spinal cord compression. International Journal of Molecular Sciences 15, 12061–73.
- <sup>360</sup> Madduri, S., Feldman, K., Tervoort, T., Papaloïzos, M., Gander, B., 2010a. Collagen nerve conduits releasing the neurotrophic factors gdnf and ngf. Journal of Controlled Release 143, 168–174. URL: <http://www.sciencedirect.com/science/article/pii/S0168365909008621>.
- <sup>365</sup> Madduri, S., di Summa, P., Papaloïzos, M., Kalbermatten, D., Gander, B., 2010b. Effect of controlled co-delivery of synergistic neurotrophic factors on early nerve regeneration in rats. Biomaterials 31, 8402–8409. URL: <http://www.sciencedirect.com/science/article/pii/S0142961210008951>.
- Müller, B., Beckmann, F., Huser, M., Maspero, F., Székely, G., Ruffieux, K., Thurner, P., Wintermantel, E., 2002. Non-destructive three-dimensional evaluation of a polymer sponge by micro-tomography using synchrotron radiation. Biomolecular Engineering 19, 73–78.
- <sup>370</sup> Müller, B., Deyhle, H., Lang, S., Schulz, G., Bormann, T., Fierz, F.C., Hieber, S.E., 2012. Three-dimensional registration of tomography data for quantification in biomaterials science. International Journal of Materials Research 103, 242–249. URL: <http://www.hanser-elibrary.com/doi/abs/10.3139/146.110663>, doi:10.3139/146.110663.
- <sup>375</sup> Otsu, N., 1979. A Threshold Selection Method from Gray-level Histograms. IEEE Transactions on Systems, Man and Cybernetics 9, 62–66. URL: <http://dx.doi.org/10.1109/tsmc.1979.4310076>, doi:10.1109/tsmc.1979.4310076.

- Schneider, C.A., Rasband, W.S., Eliceiri, K.W., 2012. Nih image to imagej: 25  
380 years of image analysis. *Nature Methods* 9, 671–675. URL: <http://dx.doi.org/10.1038/nmeth.2089>.
- Stalder, A.K., Ilgenstein, B., Chicherova, N., Deyhle, H., Beckmann, F., Müller,  
B., Hieber, S.E., 2014. Combined use of micro computed tomography and  
histology to evaluate the regenerative capacity of bone grafting materials.  
385 International Journal of Materials Research 105, 679–691. URL: <http://dx.doi.org/10.3139/146.111050>, doi:10.3139/146.111050.
- Thurner, P., Beckmann, F., Müller, B., 2004. An optimization procedure  
for spatial and density resolution in hard X-ray micro-computed tomog-  
raphy. *Nuclear Instruments and Methods in Physics Research B* 225,  
390 599–603. URL: <http://www.sciencedirect.com/science/article/pii/S0168583X04007980>.



## 2.3 Three-dimensional imaging and analysis of entire peripheral nerves after repair and reconstruction



### Highlights:

- Micro-scale details of 3D nerve fiber and vessel reorganization upon repair
- Distinct differentiation between nerve and connective tissue in a label-free manner
- Perineurium membranes and small capillaries visualized with isotropic  $4 \mu\text{m}$  resolution
- Quantitative measures proved significance for assessing repair quality,  $p < 0.01$

## Three-dimensional imaging and analysis of entire peripheral nerves after repair and reconstruction

Christos Bikis<sup>a</sup>, Lucas Degruillier<sup>b</sup>, Peter Thalmann<sup>a</sup>, Georg Schulz<sup>a</sup>, Bert Müller<sup>a</sup>, Simone E. Hieber<sup>a,\*</sup>, Daniel F. Kalbermatten<sup>c</sup>, Srinivas Madduri<sup>b,\*\*</sup>

<sup>a</sup>Biomaterials Science Center, Department of Biomedical Engineering, University of Basel, CH.;

<sup>b</sup>Center for Bioengineering and Regenerative Medicine, Department of Biomedical Engineering, University of Basel, CH.;

<sup>c</sup>Department of Plastic, Reconstructive, Aesthetic and Hand Surgery, Basel University Hospital, CH.;

---

### Abstract

*Background.* We wanted to achieve a three-dimensional (3D), non-destructive imaging and automatic post-analysis and evaluation of reconstructed peripheral nerves without involving cutting and staining processes.

*New Method.* We used a laboratory-based micro computed tomography system for imaging, as well as a custom analysis protocol. The sample preparation was also adapted in order to achieve 3D images with true micrometer resolution and suitable contrast.

*Results.* Analysis of the acquired tomograms enabled the quantitative assessment of 3D tissue structures, i.e., surface morphology, nerve fascicles, nerve tissue volume, geometry, and vascular regrowth. The resulting data showed significant differences between operated animals and non-operated controls.

---

\* Abbreviations: NC, nerve conduit;  $\mu$ CT, X-ray microtomography; ROI, region of interest; SNR, signal-to-noise-ratio;

\*\*Corresponding author at: Biomaterials Science Center, Department of Biomedical Engineering, University of Basel, Gewerbestrasse 14, 4123, Allschwil, CH. Tel.: +41 (0)61 207 5433, Fax: +41 (0)61 207 54 99

\*\*Corresponding author at: Center for Bioengineering and Regenerative Medicine, Department of Biomedical Engineering, University Hospital Basel, Spitalstrasse 21/Petersgraben 4, 4031, Basel, CH. Tel.: +41 (0)61 556 5049, Fax: +41 (0)61 265 25 25

Email addresses: [simone.hieber@unibas.ch](mailto:simone.hieber@unibas.ch) (Simone E. Hieber), [srinivas.madduri@unibas.ch](mailto:srinivas.madduri@unibas.ch) (Srinivas Madduri)

*Comparison with Existing Methods.* Our approach avoids the sampling error associated with conventional 2D visualization approaches and holds promise for automation of the analysis of large series of data sets.

*Conclusions.* We have presented a potential way for 3D imaging and analysis of entire regenerated nerves non-destructively, paving the way for high-throughput analysis of therapeutic conditions of treating adult nerve injuries.

*Keywords:*  $\mu$ CT, X-ray tomography, axonal regeneration, anatomy, morphology, micrometer, non-destructive, nerve conduits, nerve reconstruction, 3D imaging

---

## 1. Introduction

Peripheral nerve injuries constitute a medical problem of considerable significance, both in the clinic, as well as in research. Reported cases show an increasing prevalence, with several hundred thousand new patients affected annually (Kingham and Terenghi, 2006). Furthermore, the capacity of the nervous system for self-healing is *a priori* limited compared to other systems (Hsu et al., 2013). Taken together, these two factors contribute to a substantial socio-economical burden, associated with work leave, health care expenses and chronic disability.

As far as the existing therapeutic interventions are concerned, end-to-end suturing and autologous nerve grafting are the current choices of treatment (Haftek, 1976; Stang et al., 2005). Nevertheless, axonal regeneration very often remains challenging and the functional outcome is unsatisfactory. In detail, end-to-end suturing leads to a reduced stretching capacity in almost one out of four cases, due to morphological and micro-anatomical alterations at the site of the intervention. These drawbacks include the effects of Wallerian degeneration, as well as fibrosis and tissue adhesions occurring both around and inside the nerve (Kannan et al., 2005). When the direct end-to-end suturing is not an option, nerve grafting is needed, autologous grafts being the gold standard. Nevertheless, this approach is still associated with several shortcomings such

- 20 as scar formation, donor site morbidity, size and modality mismatch (Johnson et al., 2005; Weis et al., 2012).

It is for all the above reasons that research on biodegradable nerve conduits (NC) has gained increasing importance over the last 30 years (Madduri and Gander, 2012). A variety of materials are used with or without growth promoting agents, allowing for the nerve to regrow inside the NC. However, full functional recovery itself remains an unmet challenge (Yang et al., 2007; Moore et al., 2009). Furthermore, the returning of function depends to some extent on the exact 3D microanatomy of the nerve, as well as the morphology of the conduit-nerve complex. However, histology, which is the gold standard of assessing anatomical recovery, is inherently 2D. Therefore, it should ideally be complemented by a compatible, 3D approach. Currently, ultrasonography (US) and magnetic resonance imaging (MRI) are being used in clinical practice for the 3D imaging of peripheral nerves, in particular for diagnosis and for monitoring peripheral neuropathies (Garg et al., 2017; Wu et al., 2017; Walker, 2017; Willsey et al., 2017). The spatial resolution, however, is limited to a fraction of a millimeter (Willsey et al., 2017). The 3D imaging of peripheral nerves by US and MRI with true micrometer resolution, however, remains elusive.

Towards this goal, recent developments include the visualization of rat sciatic nerves by a laboratory micro computed tomography ( $\mu$ CT) system, using 40 Lugol's iodine (Hopkins et al., 2015; Pixley et al., 2016). Aiming to eliminate the need for a contrast agent, we have illustrated the use of a laboratory  $\mu$ CT system for the visualization and quantification of unstained, paraffin-embedded reconstructed nerves inside a collagen NC (Bikis et al., 2016), [Publication 1]. The visualization is perfectly compatible with histological studies based on paraffin embedding. In particular, the non-destructive micro computed tomography 45 measurements can be carried out directly after paraffin embedding and prior to the histological evaluation, with the only added process step of melting the cylindrically shaped paraffin-embedded tissue to obtain the standard histological paraffin block for the subsequent histological sectioning.

50 In this study, we have improved both the spatial resolution and contrast,

achieving high-resolution 3D imaging of regenerated nerves by using advanced laboratory-based  $\mu$ CT, where the spatial resolution was better than the distance between neighboring slices for typical histological sectioning. For this, we prepared collagen NC and implanted them in rats to bridge a 10 mm-long sciatic nerve gap injury. Three months post-operatively, regenerated nerve tissue was explanted and processed for imaging. The increase in spatial resolution was coupled with an increase in the contrast difference between anatomical structures, owing to an improved scanning and data treatment procedure. Thus, the enhanced image quality appears to be sufficient to assess the regenerated peripheral nerves in a truly 3D way, down to the true micrometer level. Hopkins et al. (2015) have already demonstrated a clear relation between the anatomical features of examined nerves recognized in micro computed tomography and histology. As consequence, the authors have focused the study on the three-dimensional CT images. For the investigated nerves, surface landmarks of the sample can also be identified, allowing for the selection of the optimal cutting plane for the histological slices (Stalder et al., 2014). This study paves the way for the standardization of the non-destructive monitoring of regenerated nerves and eventually for high throughput analysis in the field of nerve regeneration.

## 2. Materials and Methods

### 70 2.1. NC fabrication

Collagen NCs were produced using spinning mandrel technology, as illustrated previously (Madduri et al., 2010a). Insoluble collagen (2.5%, w/w) was swollen in 1 M acetic acid and then homogenized with a high-speed mixer at 10,000 rpm (Polytron<sup>®</sup>, Kinematica, Lucerne, Switzerland) for a duration of 1 minute. The homogeneous collagen dispersion was applied via a syringe onto a spinning gold-coated mandrel (diameter of 1.5 mm), installed in a sideways reciprocating apparatus, and the solvent was dried off under laminar airflow. Subsequently, the resulting tubes were neutralized by incubation in 0.1 M disodium hydrogen phosphate (pH of 7.4) for 1 hour. The tubes were finally cut

- 80 into 14 mm long specimens, which were cross-linked by subjecting the collagen tubes to a dehydro-thermal treatment (DHT) at a temperature of 110 °C and a pressure of 20 mbar for a period of 5 days. The resulting tubes exhibited an outer and inner diameter of 2.5 mm and 1.5 mm, respectively.

### 2.2. Animal experiments

- 85 All animals were treated in compliance with the ethical permission approved (25212) from the Veterinary Office of the Kanton Basel-Stadt (Basel, Switzerland). Three female Sprague Dawley rats weighing 250-300 g, about eight weeks old, were housed under standard temperature and light conditions. Left sciatic nerve was surgically operated for creating 10 mm gap. The resulting nerve gap  
90 was bridged using 14 mm collagen NC (Madduri et al., 2010b) and explanted 12 weeks post-operatively for outcome analysis. The normal nerves were collected from the un-operated side of the same animals, thus respecting the 3Rs of the animal experimentation.

### 2.3. Standard histological processing

- 95 After excision, the peripheral nerves were processed following a standard histology protocol for formalin fixation - paraffin embedding. In detail, after excision, the nerves were straightened by firmly tugging them from both ends by means of surgical forceps, fixed in histology-grade formalin, and dehydrated in ascending ethanol solutions. Subsequently, they were transferred to xylol and  
100 then perfused in a liquid paraffin-polymer mixture (Leica Paraplast). The long healthy nerve was cut in two parts and resulting segments were placed longitudinally away from each other, thus creating the gap between the two nerve segments that may represent the artificial nerve gap created in the present study. Unless otherwise stated, such gap was only for experimental characterization  
105 and excluded from the further measurement analysis.

### 2.4. Paraffin sample processing specific for X-ray imaging

When liquid paraffin perfusion was completed, the nerves were removed from the histological tissue processor, placed in a metal container and left for 24 hours

inside an oven at a temperature of 60 °C. This step is important in removing  
110 the majority of air bubbles trapped inside or around the specimen, that can cause artifacts during the X-ray imaging and make data analysis more complex. Afterwards, the specimens were thoroughly washed under flowing liquid paraffin, to remove high-absorbing particles or debris on the sample surface that would affect imaging quality. Finally, the nerve was dipped in paraffin several times  
115 while holding from one edge, until a uniform cylinder-like specimen was formed and then cooled down to 4 °C during a period of 15 minutes.

#### *2.5. Mounting of samples on holders compatible with the laboratory μCT system*

In the end, the paraffin samples were glued to specialized metal sample  
120 holders using a cyanoacrylate glue. Care was taken to ensure that the glue would cover a small area of the nerve bottom. Handling of the specimen was performed exclusively by forceps to avoid deposits on the sample surface that would cause imaging artefacts. After the glue settled, any excess was removed carefully by a scalpel and the specimens were ready for the X-ray imaging.

#### *2.6. Tomography measurements and reconstruction*

125 For the X-ray tomography measurements, we used the μCT laboratory system phoenix nanotom®m (phoenix | x-ray, GE Sensing & Inspection Technologies GmbH, Wunstorf, Germany). An acceleration voltage of 60 kV and a beam current of 280 mA were selected for the operation of the X-ray beam. Over an angular range of 360°, 1800 projections were acquired. The effective pixel size was 4 µm and scanning time was 2.5 hours for a 1 cm-long nerve. After  
130 reconstruction, the 16-bit dataset is approximately 2 GB in size.

#### *2.7. Data handling and visualization*

For the orientation within the large datasets acquired, a commercially available software is needed. The VGStudio MAX 2.1 (Volume Graphics GmbH,  
135 Heidelberg, Germany) was thus used both for the three-dimensional rendering and the visualization of the acquired tomograms, cp. images in Figures 1 and 5.

### 2.8. Data analysis

The entire process of the automated analysis is explained in detail in [Publication 1]. Shortly, the nerves were segmented from their surroundings by means of an intensity thresholding/median filtering/connected component analysis. After nerve segmentation, extraction of the investigated parameters was performed in a fully automated way. For these tasks, Matlab (MATLAB 2016a, The MathWorks, Inc., Natick, Massachusetts, United States) was used. The diagrams in Figure 3 were prepared using the pro Fit software (pro Fit 6.2.16, Quantum Soft, Uetikon am See, Switzerland). For the statistical analysis, the data were expressed as means  $\pm$  SE. Student's t test was used to determine statistical significance of differences ( $p < 0.05$  was considered statistically significant). The statistical analysis was performed in GraphPad Prism 7.00 for Mac (GraphPad Software, La Jolla California USA).

## 3. Results

### 3.1. Surface morphology

An inherent advantage of tomography with respect to traditional 2D imaging approaches is the isotropic voxel resolution provided, enabling accurate surface reconstruction, by means of 3D rendering, which is exemplarily demonstrated in the present study. In Figure 1, a healthy and a regenerated nerve are rendered, with their proximal and distal ends located at 2 mm from the right and left borders of the images, respectively.

For the reconstructed nerve, starting near its proximal end, the marking sutures and the scarring that has occurred around them are visible (yellow-colored arrow). Muscle fibers attached to the nerve surface (white-colored arrow) are also visible close to the proximal nerve end. The middle section of the reconstructed nerve shows a reduced diameter with respect to the ends. A line plot of the cross sectional area is presented below. The distal nerve end is presented in larger magnification in Figure 1(b, bottom), which shows how the fibrinoid tissue envelops the sutures.

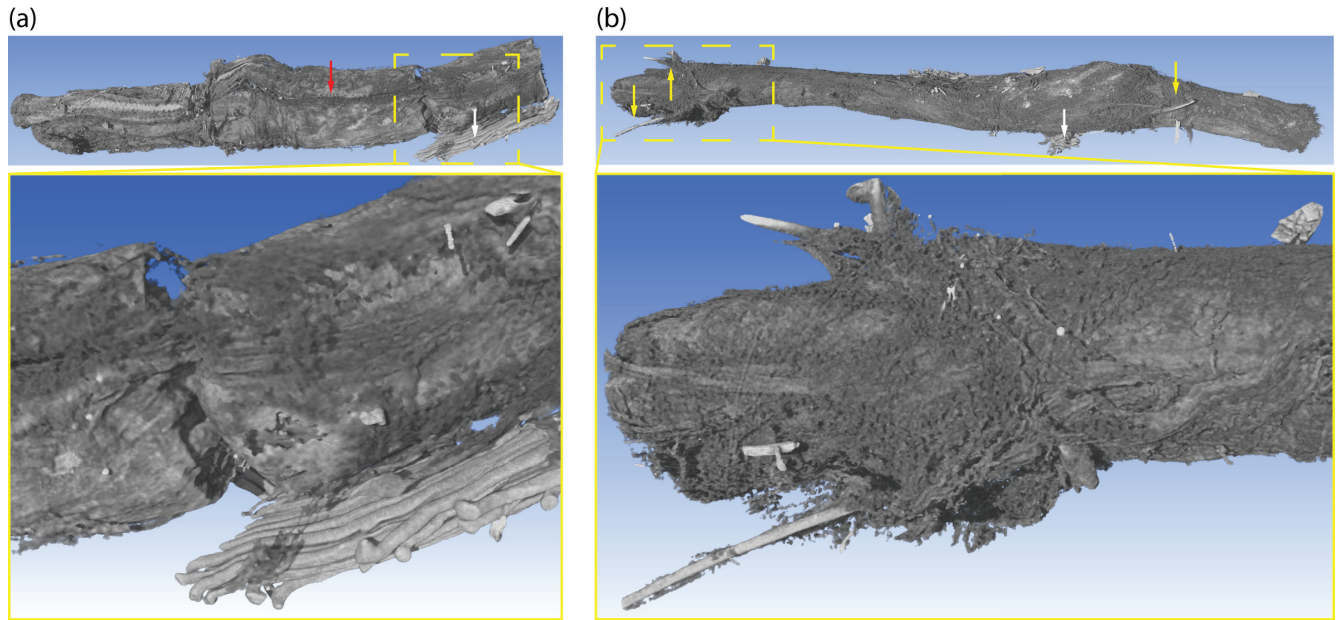


Figure 1: Three dimensional visualization of tomography data from a healthy (a) and a reconstructed nerve (b), with a length of approximately 8 and 15 mm, respectively. The surrounding paraffin has been made digitally transparent prior to this 3D rendering. The red-colored arrow indicates the surface groove between the major nerve fascicles and the white-colored arrows show muscle fibers on the surface of the nerves. The yellow-colored arrows indicate the two ends of the reconstructed nerve.

For the overview image of the healthy nerve (Fig. 1a, top), presented for comparison, the most prominent difference to the reconstructed nerve is the major surface groove (red arrow) caused by the existence of two main nerve fascicles. More muscle fibers are seen attached to the nerve surface (white-colored arrow), compared to the regenerated nerve. The mean diameter of these muscle fibers is around  $50 \mu\text{m}$ , in reasonable agreement with the literature values (Alnaqeeb and Goldspink, 1987). A zoom-in onto the surface of the healthy nerve (Fig. 1a, bottom) better reveals their rod-like structure and parallel arrangement.

### 3.2. Structural analysis of reconstructed nerve

Another distinctive advantage of 3D tomographic data is the ability to select any virtual cutting plane, as illustrated in Figure 2, where three orthogonal cutting planes at once are used to better reveal the internal structures and the degree of organization of the nerves investigated. The white color structures appearing in longitudinal and cross-sectional images of both nerve samples indicate the axons and associated myelin tissue (Hopkins et al., 2015; Pixley et al., 2016). Fission-like-structures existing in the cross sections show the organization of the nerve fascicles in all the tissue samples. The epineurium and perineurium membranes as well as the vessels are depicted white, due to a higher local X-ray absorption, while the surrounding medium (air) is shown as black, due to minimal X-ray absorption. Paraffin surrounding the nerves is shown in gray, according to the local X-ray absorption.

For the reconstructed nerve data, the cross-sectional view obtained from its proximal end, reveals the existence of two main nerve fascicles, divided by one prominent perineurium membrane. No major vessel can be detected in this cross-sectional view, as easy as in the healthy nerve (Fig. 2). In addition, the connective tissue surrounding the fascicles is enveloping them more closely than for the case of the healthy nerve, where both the connective tissue and the epineurium membrane are separated from the four main nerve fascicles visible and at places show differing X-ray absorption.

The longitudinal views clearly revealed the internal structures such as the fascicle orientation and 3D organization. In the reconstructed nerves, the fascicles are not as easily distinguishable, as it is the case for their healthy counterpart. Moreover, the reconstructed nerve shows a random arrangement of fascicles, that, especially around its proximal and distal end becomes so complicated that some of them are perpendicular to the major nerve axis. Both nerve thickness and degree of fascicle anisotropy are maximized at the proximal and distal nerve ends, compared to its thinner middle section.

Figure 2 also shows two line plots through the selected cross sectional cuts of the 3D dataset, indicating a spatial resolution close to the effective pixel

size for both measurements. Histograms of the local X-ray absorption from selected regions of the two datasets are also presented. They contain three Gaussian peaks corresponding to air (red), paraffin (green) and nerve tissue (blue), which can be identified by intensity thresholding (Müller et al., 2002).  
210The area under the histogram curve includes all voxels of the selected region of interest (ROI), and the area under each peak provides the volume of its related specimen component. For our measurements, the fact that the Gaussians fit the data very well indicates the meaningful applicability of photon statistics. For each Gaussian, the expectation value  $\mu$  gives the peak position corresponding to a specific component and the standard deviation  $\sigma$  characterizes how broad the distribution is. Based on these parameters, the Signal-to-Noise Ratio (SNR) of each specific component was calculated as:  $\text{SNR}(\text{component}) = |\mu_{\text{component}} - \mu_{\text{air}}| / \sigma_{\text{air}}$ . The SNR for both paraffin and nerve was almost equal for both measurements (  $\text{SNR}_{\text{healthy}}(\text{paraffin}) = 34.31 \pm 0.02$  ;  $\text{SNR}_{\text{regenerated}}(\text{paraffin}) = 37.12 \pm 0.02$ ,  $\text{SNR}_{\text{healthy}}(\text{nerve}) = 47.99 \pm 0.03$  ;  $\text{SNR}_{\text{regenerated}}(\text{nerve}) = 44.74 \pm 0.03$  ).  
215  
220

### 3.3. Nerve thickness profile

After the nerve has been segmented from its surrounding paraffin, plotting the cross-sectional area over the nerve length provides useful information on the nerve regeneration process, as seen in Figure 3, where one representative healthy and one reconstructed nerve are presented from each group. There are two distinctive peaks in the curve of the reconstructed nerve, indicating the proximal (left) and distal (right) end. The region between these two peaks corresponds to the reconstructed nerve segment. For the case of a healthy nerve, its thickness profile revealed by measurement of cross-sectional area remains relatively constant along its entire length.  
225  
230

### 3.4. Nerve geometry

We have also calculated several geometrical parameters for the nerves investigated, in an automated process. Figure 4 shows the results of the two groups  
235

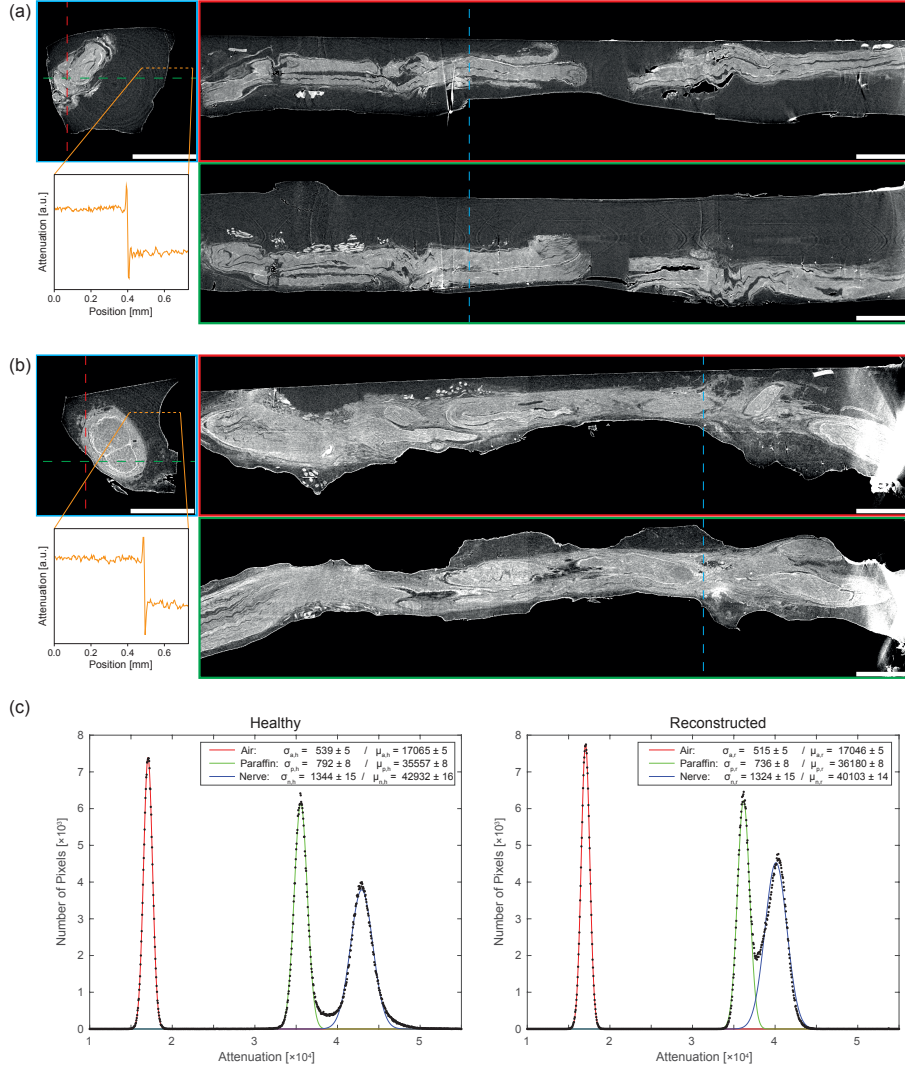


Figure 2: Cross sectional and longitudinal views of healthy (a) and regenerated (b) rat sciatic nerves respectively, together with selected line plots and histograms of selected regions of interest (c). The green, red and blue dashed lines and subfigure frames show the relative position of the depicted cuts through the 3D datasets. The included line plots are taken along the orange-colored dashed lines. In the longitudinal views, the proximal and distal ends of the nerves are located at 2 mm from the right and left borders of the images, respectively. In these views, one recognizes that the healthy nerve is comprised of two parts, which show only a small gap and are embedded into paraffin together. The black dots in the histogram indicate the number of pixels corresponding to a specific attenuation value and the curves are Gaussians fitted to the experimental data, corresponding to air (red), paraffin (green) and nerve (blue). The attenuation values are related to the current setup and do not represent the physical quantity used for monochromatic radiation. The scale bars correspond to a length of 1 mm.

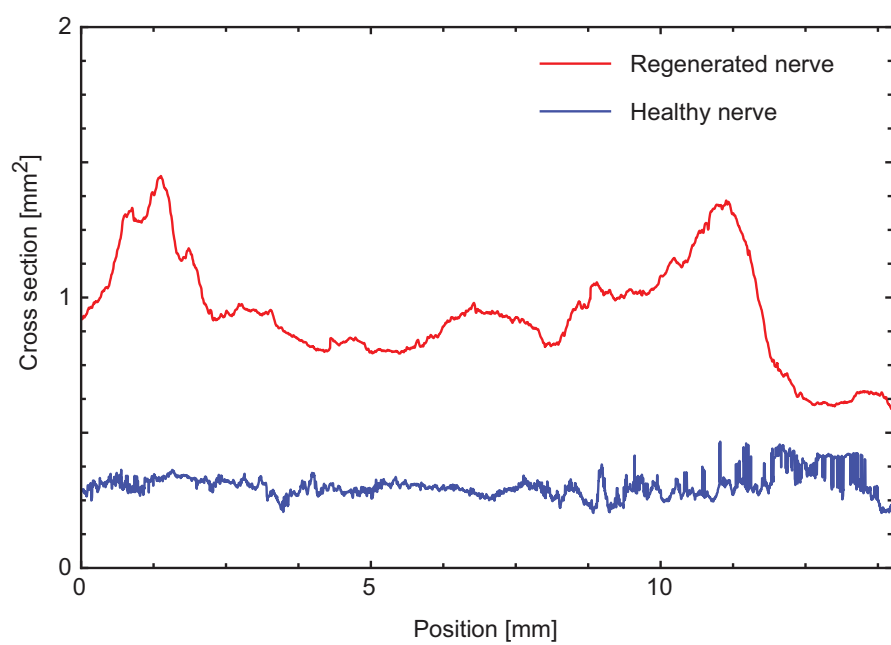


Figure 3: Cross sectional area along two representative nerves. The healthy nerve shows an almost constant value, whereas the regenerated nerve exhibits characteristic modulations.

of healthy and reconstructed nerves ( $n=3$ ), as well as their comparison. The parameters chosen for the investigation were the median and maximum cross section, the average cross sections (defined as volume/length), the half mid-range crossection (defined as the distance of maximum to the median) and the cross section abs mid-range (defined as the sum of the distance of each cross section along the nerve length to the median). In detail, a strongly statistically significant difference was observed between the reconstructed and the healthy group for the median cross section ( $p = 0.0026$ ). There was also a statistically significant difference between the two groups for the average cross section (defined as volume/length) and the cross section abs (absolute) mid-range (defined as the sum of the distance of the cross section at each position along the nerve to the median cross section), with  $p = 0.0178$  and  $p = 0.0419$ , respectively. Finally, a tendency for a statistically significant difference between the two groups was found for the maximum cross section ( $p = 0.0890$ ).

**250 3.5. Vascular regrowth**

Vessels show a higher intensity value than paraffin or nervous tissue, namely around 44000 for the histograms presented in Figure 2. Due to a low number of vessel voxels the histogram does not reveal them separately. The vessel network is visualized in Figure 5 using thresholding. Intensity thresholding revealed interesting observations associated with vascular regrowth. The results of this segmentation process are seen in Figure 5, revealing the vascular network of a healthy (Fig. 5a) and reconstructed (Fig. 5b) nerve, respectively. In detail, for the case of the reconstructed nerves, the mean diameter of the detected vessels is smaller, compared to healthy nerves. In addition, a quick overview of the reconstructed nerve (Fig. 5b) revealed the existence of several small signals characterized by high X-ray absorption at the proximal and distal nerve ends (green-colored arrows). These structures may indicate haematomas.

Inside the reconstructed nerve, the morphology and organization of vessels appeared to be heterogeneous. The visual inspection of the high-resolution CT data indicates that the nerve ends contain a less organized vessel structure and

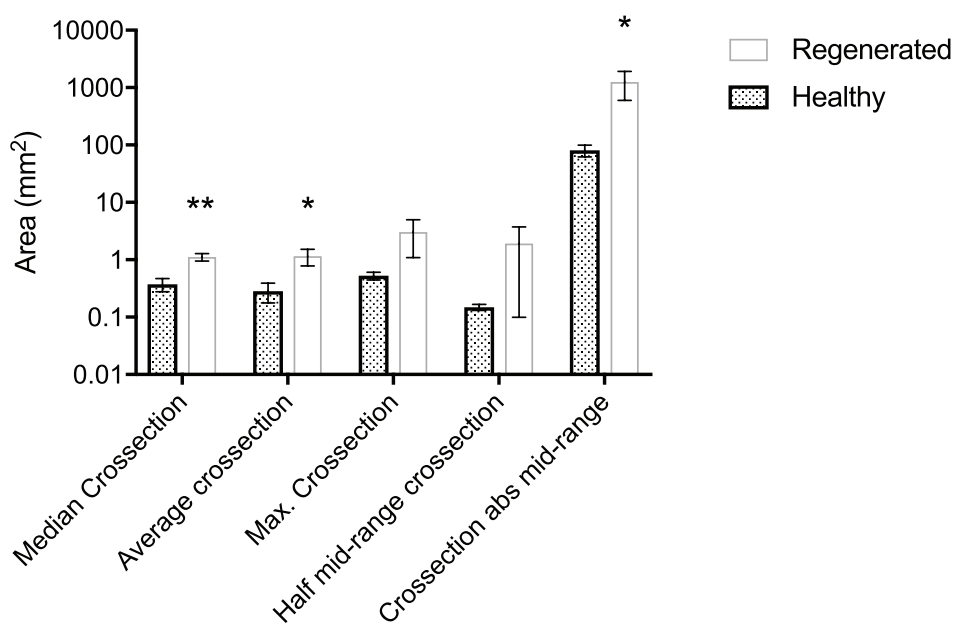


Figure 4: Comparison of geometrical parameters for three healthy and three regenerated nerves, calculated automatically after nerve segmentation. Single asterisk indicates a  $p$ -value smaller than 0.05 and double asterisk indicates a  $p$ -value smaller than 0.01.

have random orientation. It is difficult to prove this observation, since the number of segmented vessels is relatively low. Vessel density is also higher near the two ends of the nerve. In contrast, the region between the proximal and distal parts of the reconstructed nerve exhibits a more organized vessel structure; 270 vessels are generally bigger in diameter compared to the ones at the nerve ends and are less frequently branched. They are mostly parallel one to another, following the nerve axis and residing very close to its surface (magenta-colored arrow).

#### 4. Discussion

##### 275 4.1. Spatial resolution and image contrast

The lineplots presented in Figure 2 run along the paraffin/air edge and were used to determine the spatial resolution close to the pixel size, as described earlier (Thurner et al., 2004). From the mean and standard deviation values of the Gaussians fitted to the histograms presented in Figure 2, the SNR for 280 the microstructures was calculated (Schulz et al., 2012). The SNR was almost identical for the case of paraffin (considered to be a homogeneous structure) in both measurements. Together with the fact that spatial resolution was also found similar for both measurements, scanning quality is considered consistent. Compared to US and MRI, which are the modalities of choice for peripheral 285 nerve 3D imaging in clinical practice (Willsey et al., 2017), the spatial resolution achieved in this study is at least two orders of magnitude better in each of the three orthogonal directions. Compared to recent similar  $\mu$ CT studies, e.g. Hopkins et al. (2015); Pixley et al. (2016), spatial resolution is at least an order of magnitude better in each orthogonal direction. Although our approach needs no 290 staining agent at all, the obtained tomogram contrast is also greatly increased, allowing for the discrimination between nerve fascicles and connective tissue, an unsolved problem for similar studies up until now (Hopkins et al., 2015). The superior image quality makes even an automated nerve segmentation and extraction of quantitative parameters possible.

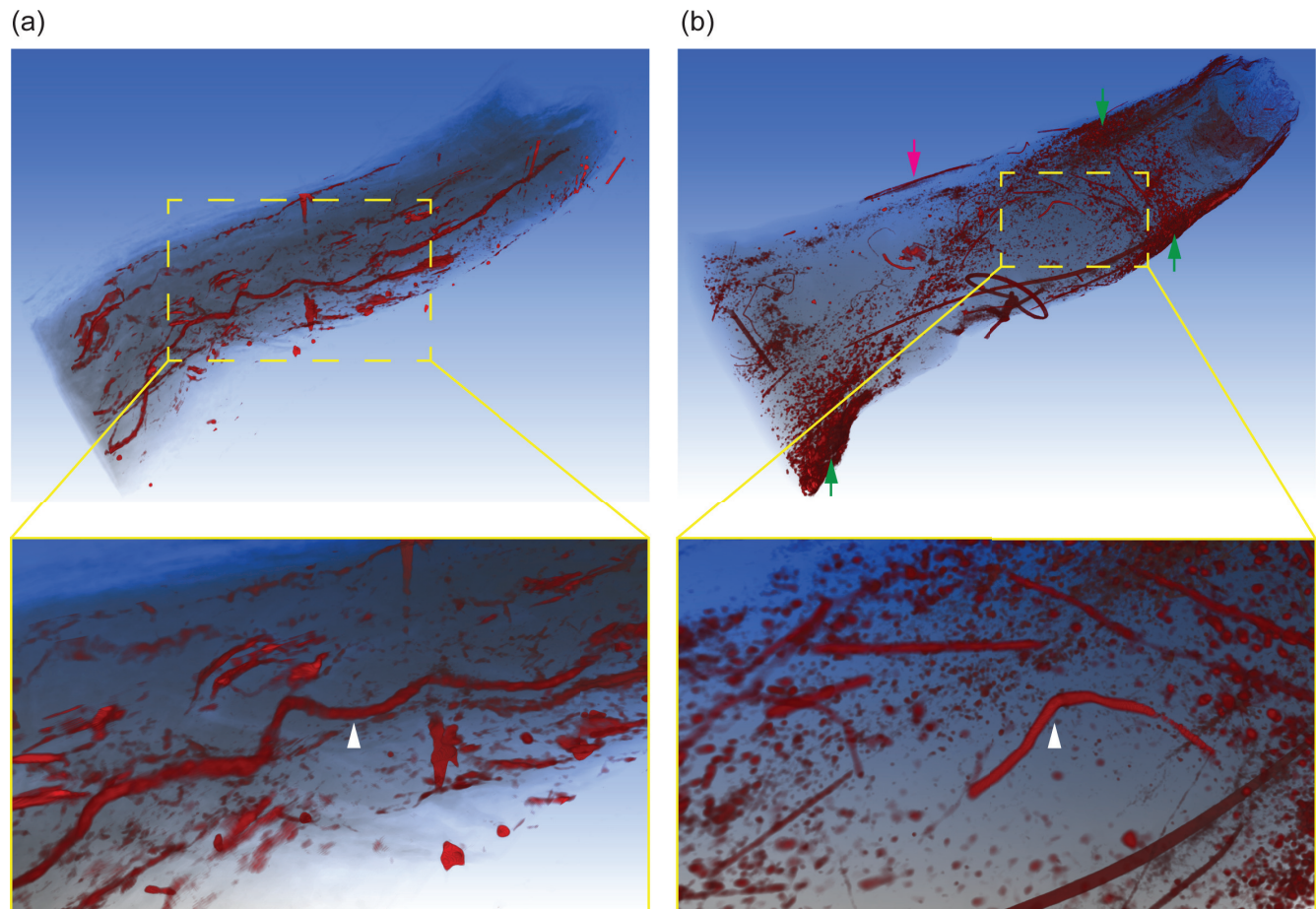


Figure 5: Intensity-thresholded vessels of a healthy (a) and a reconstructed (b) nerve, with a length of approximately 3 and 7 mm, respectively. The surrounding paraffin has been made digitally transparent and the nerve volume has been made semi-transparent to allow for a better visualization of the vessel structure. The diameter of the vessels indicated by the white-colored arrows is approximately 0.04 and 0.02 mm for the healthy and the reconstructed nerve, respectively.

**295** In this study, the most notable difference between the two measurements is the better separation of the paraffin and nerve peak of the histograms for the case of the healthy nerve compared to the regenerated one, as seen in the images of Figure 2. We have already some indications that during the first days of the sample being embedded in paraffin, contrast difference between structures  
**300** increases as the time passes, most probably due to an ongoing perfusion progress. It is also possible, that a combination of an existing difference between groups and a preparation effect could have taken place; one hypothesis is, that the regenerating nerve, due to less compact bundle packing or myelin maturity, is physically less stable and therefore gets more affected during the dehydration  
**305** and subsequent paraffin perfusion.

#### *4.2. Thickness profile along the nerves*

Diagrams as shown in Figure 3 can be used to assess the length of the zones in the regenerating nerves, as well as quickly reveal possible segmentation errors. For example, the numerous small spikes of the cross-sectional area along the end  
**310** of the healthy nerve were caused by suboptimal segmentation, due to cone beam artefacts.

While the fast fluctuations in the amplitude are caused by improper segmentation, the high and slow modulation of the regenerating nerve cross section compared to its healthy counterpart can be explained by the mechanism  
**315** of nerve damage and regeneration itself. An increased cross-sectional area is seen, as expected, in the proximal and distal ends of the reconstructed nerve, which may indicate occurrence of hemorrhage, inflammation and scarring (Fig. 3). Also as expected, the regenerated area is found to be relatively thinner, as seen for the case of the sample displayed in Figure 1b. The two bundles  
**320** observed in the cross-sectional view are not well separated and are ultimately joined further along the nerve, so that at the thinnest part of the regenerated region, all fascicles are enclosed by one single perineurium membrane.

#### *4.3. Geometry of reconstructed nerve tissue*

It should be noted that the calculated nerve cross-sectional area was taken  
325 with respect to the plane perpendicular to the rotation axis of the sample and  
not to the nerve centerline. For our case this only has a minor effect on the  
results, because the nerves were straightened as much as possible prior to em-  
bedding and then mounted with the major nerve axis parallel to the rotation  
axis. Even though the median cross section has the strongest difference between  
330 the two groups in terms of statistical significance, the average cross section (vol-  
ume/length) can sometimes be a more preferable parameter for comparison,  
since it is more robust with respect to how the sample is embedded or mounted.

Cross section abs mid-range is a more robust parameter compared to the  
half mid-range cross section because it ignores the intra-group differences in  
335 nerve size and is directly affected by the existence of transition zones in the  
regenerated nerves. This is because the former takes the difference of the cross  
section at every point along the nerve compared to its median cross section,  
while the later is merely the difference of only two values, namely maximum  
and median cross section of the nerve.

340 To be able to compare geometrical parameters, all muscle or connective  
tissue around the nerve has to be cleared as much as possible during extraction.  
The regenerated nerves must also be cut with similar endpoints, e.g. using the  
stitches as guides.

#### *4.4. Interpretation and challenges of vessel analysis*

345 The visual inspection of the CT data indicates that vessels smaller than  
the voxel size can be detected due to the partial volume effect. Their high  
intensity is mainly a result of the remaining dehydrated blood in the vessel  
lumen. An elaborate, automated segmentation of the entire vessel tree remains  
an open challenge. Given that no contrast agent was used, the non-connected  
350 vessel network visualized can be caused by inhomogeneous vessel perfusion by  
paraffin, probably due to trapped air inside the vessels. Nevertheless, there is  
a clear tendency for more, shorter vessel fragments in the reconstructed nerve

ends that can be explained by the angiogenesis at this sites as a response to trauma and as a basis for subsequent regeneration. In addition to that, it is  
355 very probable that the highly X-ray absorbing features filling large areas at the reconstructed nerve ends are caused by haemosidirin deposits due to hemorrhage at these areas.

### 5. Conclusions

We have achieved a 3D visualization of regenerated nerves with true micrometer resolution using a procedure that allows subsequent cutting and staining.  
360 Fine details of morphology and microanatomy of nerve tissue were visualized, owing to improved imaging procedure and an updated data processing. The method has been validated with a sufficient number of samples to provide findings with statistical significance. The quantitative parameters of regenerated  
365 nerves detailed in this study provide a suitable measure for assessing the quality of nerve regeneration with a focus on high-throughput analysis.

### 6. Acknowledgments

The authors thank Stephan Frank and Jürgen Hench of the Neuropathology Department, Basel University Hospital for allowing the use of histological  
370 equipment, as well as Sascha Martin and Stefan Gentsch of the Mechanics Shop, Physics Department, University of Basel, for fabricating the customized sample holders. The project was supported by SNSF projects 144535 and 133802.

### 7. Conflicts of interest

The authors declare no conflict of interest

### 375 References

- Alnaqeeb, M.A., Goldspink, G., 1987. Changes in fibre type, number and diameter in developing and ageing skeletal muscle. *Journal of Anatomy* 153, 31–45. URL: <http://www.ncbi.nlm.nih.gov/pmc/articles/PMC1261780/>.

- Bikis, C., Degruillier, L., Deyhle, H., Schulz, G., Schweighauser, G., Hench, J., Müller, B., Madduri, S., Hieber, S.E., 2016. Using laboratory  $\mu$ CT for assessing peripheral nerve regeneration. European Cells and Materials 32, 30.
- Garg, K., Aggarwal, A., Srivastava, D.N., Jana, M., Sharma, R., Gamanagatti, S., Kumar, A., Kumar, V., Malhotra, R., Goyal, V., Garg, K., 2017. Comparison of different sequences of mri and ultrasongram with nerve conduction studies in peripheral neuropathies. World neurosurgery .
- Haftek, J., 1976. Autogenous cable nerve grafting instead of end to end anastomosis in secondary nerve suture. Acta Neurochirurgica (Wien) 34, 217–21.
- Hopkins, T.M., Heilman, A.M., Liggett, J.A., LaSance, K., Little, K.J., Hom, D.B., Minteer, D.M., Marra, K.G., Pixley, S.K., 2015. Combining micro-computed tomography with histology to analyze biomedical implants for peripheral nerve repair. Journal of Neuroscience Methods 255, 122–30.
- Hsu, S.H., Kuo, W.C., Chen, Y.T., Yen, C.T., Chen, Y.F., Chen, K.S., Huang, W.C., Cheng, H., 2013. New nerve regeneration strategy combining laminin-coated chitosan conduits and stem cell therapy. Acta Biomaterialia 9, 6606–15.
- Johnson, E.O., Zoubos, A.B., Soucacos, P.N., 2005. Regeneration and repair of peripheral nerves. Injury 36 Suppl 4, S24–9.
- Kannan, R.Y., Salacinski, H.J., Butler, P.E.M., Seifalian, A.M., 2005. Artificial nerve conduits in peripheral-nerve repair. Biotechnology and Applied Biochemistry 41, 193–200.
- Kingham, P.J., Terenghi, G., 2006. Bioengineered nerve regeneration and muscle reinnervation. Journal of Anatomy 209, 511–526. URL: <http://www.ncbi.nlm.nih.gov/pmc/articles/PMC2100355/>.
- Madduri, S., Feldman, K., Tervoort, T., Papaloïzos, M., Gander, B., 2010a. Collagen nerve conduits releasing the neurotrophic factors gdnf and ngf. Journal

of Controlled Release 143, 168–174. URL: <http://www.sciencedirect.com/science/article/pii/S0168365909008621>.

Madduri, S., Gander, B., 2012. Growth factor delivery systems and repair strategies for damaged peripheral nerves. Journal of Controlled Release 161,  
410 274–82.

Madduri, S., di Summa, P., Papaloïzos, M., Kalbermatten, D., Gander, B.,  
2010b. Effect of controlled co-delivery of synergistic neurotrophic factors on  
early nerve regeneration in rats. Biomaterials 31, 8402–8409. URL: <http://www.sciencedirect.com/science/article/pii/S0142961210008951>.

415 Moore, A.M., Kasukurthi, R., Magill, C.K., Farhadi, H.F., Borschel, G.H.,  
Mackinnon, S.E., 2009. Limitations of conduits in peripheral nerve repairs.  
Hand (New York, N.Y.) 4, 180–6.

Müller, B., Thurner, P., Beckmann, F., Weitkamp, T., Rau, C., Bernhardt, R.,  
Karamuk, E., Eckert, L., Brandt, J., Buchloh, S., Wintermantel, E., Scharn-  
420 weber, D., Worch, H., 2002. Nondestructive three-dimensional evaluation  
of biocompatible materials by microtomography using synchrotron radiation.  
Proceedings of SPIE 4503, 178–188. URL: <http://dx.doi.org/10.1117/12.452843>, doi:10.1117/12.452843.

Pixley, S.K., Hopkins, T.M., Little, K.J., Hom, D.B., 2016. Evaluation of pe-  
425 ripheral nerve regeneration through biomaterial conduits via micro-ct imag-  
ing. Laryngoscope investigative otolaryngology 1, 185–190.

Schulz, G., Weitkamp, T., Zanette, I., Pfeiffer, F., Müller-Gerbl, M., David, C.,  
Müller, B., 2012. Asymmetric rotational axis reconstruction of grating-based  
x-ray phase contrast tomography of the human cerebellum. Proceedings of  
430 SPIE 8506, 850604. URL: <http://dx.doi.org/10.1117/12.928487>, doi:10.  
1117/12.928487.

Stalder, A.K., Ilgenstein, B., Chicherova, N., Deyhle, H., Beckmann, F., Müller,  
B., Hieber, S.E., 2014. Combined use of micro computed tomography and

- histology to evaluate the regenerative capacity of bone grafting materials.
- <sup>435</sup> International Journal of Materials Research 105, 679–691. URL: <http://dx.doi.org/10.3139/146.111050>, doi:10.3139/146.111050.
- Stang, F., Fansa, H., Wolf, G., Reppin, M., Keilhoff, G., 2005. Structural parameters of collagen nerve grafts influence peripheral nerve regeneration. *Biomaterials* 26, 3083–91.
- <sup>440</sup> Thurner, P., Beckmann, F., Müller, B., 2004. An optimization procedure for spatial and density resolution in hard X-ray micro-computed tomography. *Nuclear Instruments and Methods in Physics Research B* 225, 599–603. URL: <http://www.sciencedirect.com/science/article/pii/S0168583X04007980>.
- <sup>445</sup> Walker, F.O., 2017. Ultrasonography in peripheral nervous system diagnosis. *Continuum (Minneapolis, Minn.)* 23, 1276–1294.
- Weis, J., Brandner, S., Lammens, M., Sommer, C., Vallat, J.M., 2012. Processing of nerve biopsies: a practical guide for neuropathologists. *Clinical Neuropathology* 31, 7–23.
- <sup>450</sup> Willsey, M., Wilson, T.J., Henning, P.T., Yang, L.J.S., 2017. Intraoperative ultrasound for peripheral nerve applications. *Neurosurgery clinics of North America* 28, 623–632.
- Wu, C., Wang, G., Zhao, Y., Hao, W., Zhao, L., Zhang, X., Cao, J., Wang, S., Chen, W., Chan, Q., Zhao, B., Chhabra, A., 2017. Assessment of tibial and common peroneal nerves in diabetic peripheral neuropathy by diffusion tensor imaging: a case control study. *European radiology* 27, 3523–3531.
- <sup>455</sup> Yang, Y., Ding, F., Wu, J., Hu, W., Liu, W., Liu, J., Gu, X., 2007. Development and evaluation of silk fibroin-based nerve grafts used for peripheral nerve regeneration. *Biomaterials* 28, 5526–35.



### 3 Conclusions

The experimental data from the synchrotron-radiation measurements demonstrate a smaller difference in contrast between absorption- and phase-contrast tomography, than the one expected. Such a discrepancy could, at least partially, be caused by the limitation of the current experimental setups in detecting the broad ranges of the real and imaginary part of the refractive index of a multi-component biological sample during a single measurement. It is also important to note that previous comparisons between the two modalities have considered the same energy for both measurements, optimized for the case of phase-contrast. Contrarily, we chose a different photon energy for the two measurements optimized for both phase-, as well as absorption-contrast, based on the specimen geometry and physical composition, as described previously [21]. The effect of the dehydration that precedes paraffin embedding, in increasing the specimen density must also not be overlooked.

The quantitative synchrotron results were further verified by the laboratory  $\mu$ CT measurements of FFPE peripheral nervous tissue, exhibiting a high quality of data that even allowed for automatic segmentation of structures of interest and extraction of parameters for the assessment of nerve regeneration. It was also shown that such laboratory experiments can even be correlated to a single SR $\mu$ CT measurement, to extract more information for several investigated samples. An initial phase dataset can be used, e.g., to obtain the absorption coefficient values of an anatomical structure of interest in an entire series of absorption measurements. The specialized paraffin embedding protocol, reconstruction algorithms and computational analysis tools developed during this study, aim to offer a complete pipeline for efficient, high-quality 3D investigations of FFPE tissue, which is perfectly compatible with the standard histological processing.

Several results of this study have already been effectively put in use for other studies, including among others: (a) employing the specialized paraffin embedding protocol for specimens being used for the three dimensional investigation of FFPE human brain tissue beyond the optical limit, (b) implementing the adapted scanning procedure related to sensitive FFPE mouse brain specimens for the investigation of tumor vasculature, as well as the comparison of the single- and double-grating phase modalities (c) using the SR-based data post-processing and reconstruction algorithms developed during this work for other anatomical and functional SR $\mu$ CT studies.

Last but not least additional collaborations with research- and clinically-oriented partners are already established in order to reproduce the very promising results of laboratory-based absorption  $\mu$ CT in other biomedical applications related to the investigation of nervous tissue. For the case of the central nervous system, we aim to investigate the anatomical alterations that occur in the human and mouse epileptic brain, in collaboration with the Neurosurgery and Neuropathology Departments of

the Basel University Hospital and the Experimental Epilepsy Research Center of the University Hospital Freibourg, Germany. Moreover, exploiting our knowledge on the visualization of peripheral nerves, we are planning to employ laboratory  $\mu$ CT for the faster and more efficient diagnosis of vasculitis based on sural nerve biopsy.

## Bibliography

- [1] U. Bonse and M. Hart, “*An X-ray interferometer*”, Applied Physics Letters, 6(8), 155–156 (1965).
- [2] F. J. Momose, A., “*Phase-contrast radiographs of nonstained rat cerebellar specimen*”, Medical Physics, 22, 375–9 (1995).
- [3] U. Bonse, “*Röntgen-Mikrotomographie*”, Physik Journal, 53(3), 211–214 (1997).
- [4] A. Momose, T. Takeda, Y. Itai, K. Hirano, and A. Yoneyama, “*Phase-contrast x-ray imaging using an x-ray interferometer*”, Synchrotron Radiation News, 11(5), 27–32 (1998).
- [5] M. J. Kitchen, G. A. Buckley, T. E. Gureyev, M. J. Wallace, N. Andres-Thio, K. Uesugi, N. Yagi, and S. B. Hooper, “*CT dose reduction factors in the thousands using X-ray phase contrast*”, Scientific Reports, 7(1), 15953 (November 2017).
- [6] G. Schulz, T. Weitkamp, I. Zanette, F. Pfeiffer, F. Beckmann, C. David, S. Rutishauser, E. Reznikova, and B. Müller, “*High-resolution tomographic imaging of a human cerebellum: comparison of absorption and grating-based phase contrast*”, Journal of the Royal Society Interface, 7(53), 1665–1676 (2010).
- [7] A. Lareida, F. Beckmann, A. Schrott-Fischer, R. Glueckert, W. Freysinger, and B. Müller, “*High-resolution X-ray tomography of the human inner ear: synchrotron radiation-based study of nerve fibre bundles, membranes and ganglion cells.*”, Journal of Microscopy, 234, 95–102 (2009).
- [8] M. Zamir, J. Twynstra, A. J. Vercnocke, I. Welch, S. M. Jorgensen, E. L. Ritman, D. W. Holdsworth, and J. K. Shoemaker, “*Intrinsic microvasculature of the sciatic nerve in the rat.*”, Journal of the Peripheral Nervous System, 17, 377–84 (2012).
- [9] S. E. Hieber, C. Bikis, A. Khimchenko, G. Schweighauser, J. Hench, N. Chicherova, G. Schulz, and B. Müller, “*Tomographic brain imaging with nucleolar detail and automatic cell counting*”, Scientific Reports, 6, 32156 (2016).
- [10] A. Khimchenko, H. Deyhle, G. Schulz, G. Schweighauser, J. Hench, N. Chicherova, C. Bikis, S. E. Hieber, and B. Müller, “*Extending two-dimensional histology into the third dimension through conventional micro computed tomography.*”, NeuroImage, 139, 26–36 (2016).
- [11] P. J. Kingham and G. Terenghi, “*Bioengineered nerve regeneration and muscle reinnervation*”, Journal of Anatomy, 209(4), 511–526 (2006).

- [12] S.-H. Hsu, W.-C. Kuo, Y.-T. Chen, C.-T. Yen, Y.-F. Chen, K.-S. Chen, W.-C. Huang, and H. Cheng, “*New nerve regeneration strategy combining laminin-coated chitosan conduits and stem cell therapy.*”, *Acta Biomaterialia*, 9, 6606–15 (2013).
- [13] J. Haftek, “*Autogenous cable nerve grafting instead of end to end anastomosis in secondary nerve suture.*”, *Acta Neurochirurgica (Wien)*, 34, 217–21 (1976).
- [14] F. Stang, H. Fansa, G. Wolf, M. Reppin, and G. Keilhoff, “*Structural parameters of collagen nerve grafts influence peripheral nerve regeneration.*”, *Biomaterials*, 26, 3083–91 (2005).
- [15] R. Y. Kannan, H. J. Salacinski, P. E. M. Butler, and A. M. Seifalian, “*Artificial nerve conduits in peripheral-nerve repair.*”, *Biotechnology and Applied Biochemistry*, 41, 193–200 (2005).
- [16] E. O. Johnson, A. B. Zoubos, and P. N. Soucacos, “*Regeneration and repair of peripheral nerves.*”, *Injury*, 36 Suppl 4, S24–9 (2005).
- [17] J. Weis, S. Brandner, M. Lammens, C. Sommer, and J.-M. Vallat, “*Processing of nerve biopsies: a practical guide for neuropathologists.*”, *Clinical Neuropathology*, 31, 7–23 (2012).
- [18] S. Madduri and B. Gander, “*Growth factor delivery systems and repair strategies for damaged peripheral nerves.*”, *Journal of Controlled Release*, 161, 274–82 (Jul 2012).
- [19] Y. Yang, F. Ding, J. Wu, W. Hu, W. Liu, J. Liu, and X. Gu, “*Development and evaluation of silk fibroin-based nerve grafts used for peripheral nerve regeneration.*”, *Biomaterials*, 28, 5526–35 (2007).
- [20] A. M. Moore, R. Kasukurthi, C. K. Magill, H. F. Farhadi, G. H. Borschel, and S. E. Mackinnon, “*Limitations of conduits in peripheral nerve repairs.*”, *Hand* (New York, N.Y.), 4, 180–6 (2009).
- [21] L. Grodzins, “*Optimum energies for x-ray transmission tomography of small samples: Applications of synchrotron radiation to computerized tomography I*”, *Nucl. Instr. Meth. Phys. Res.*, 206(3), 541–545 (1983).

## Acknowledgements

First and foremost, since the very beginning of its conception, this entire project has only been possible due to the will, constant support and unwavering faith of my Doktorvater Bert Müller. I simply cannot thank him enough as a supervisor and a co-worker for his great personal effort and time. His door was always open and he was there to support his students in any way possible, from teaching and posing intriguing scientific questions that needed to be answered to simply offering practical support and advice. Even more importantly, he always encouraged me to express my own mind, even if he knew beforehand that he would not agree. Under his mentoring I have grown both scientifically and as a person and for that I am deeply grateful.

Looking back at this exciting journey that my PhD has been, I want to wholeheartedly thank all BMC members for making me feel right at home from the very day of my interview, even before I joined our group. I can only hope that my future working environments will be as good. At this point, I also feel the need to thank so many people, whose contributions, small and large alike, have made this work possible.

- For supporting the project and having a supervising role:

Alex Dommann for kindly agreeing to act as a co-referee and evaluate my thesis.

Raphael Guzman, Luigi Mariani, Srinivas Madduri, Carola Haas, Stamatios Theocharis and Markus Rudin for their kind support of the project and their eagerness to get involved in fruitful collaborations.

Stephan Frank for his support of the project and for offering the idea of employing  $\mu$ CT for vasculitis diagnosis.

Simone Hieber for sharing the supervision of my project and providing crucial help related to the project proposal and study formulation.

Dirk Bumann, Gerhard Christofori, Christoph Hess, Nancy Hynes, Anne Spang and Jörg Schwaller for offering their input and constructive criticism on my MD-PhD proposal.

- For working closely with, and learning from them:

Peter Thalmann for immensely supporting with synchrotron data reconstruction and analysis, for the stimulating Physics discussions, and among others, for spending his 2016 Christmas holidays to help me with my first two manuscripts. It was a real privilege to work with him.

Jürgen Hench for taking a lot of his valuable time to introduce me to the histological preparation procedures, share his extensive knowledge in Pathology and his enthusiasm for science and research in general. The discussions with him were always both extremely interesting and immensely helpful and he has also greatly contributed to identifying medical problems that could be addressed by  $\mu$ CT.

Georg Schulz and Hans Deyhle for showing me how to perform X-ray measurements, both in the synchrotron and laboratory and for tolerating my endless questions, especially during the early morning hours of the synchrotron night shifts.

Griffin Rodgers, who has offered crucial help during the experiments, data analysis and manuscript preparation for my third publication. It is a pity that we could not work together for a longer time, since he only joined the BMC shortly before the end of my thesis.

Gabriel Schweighauser for introducing me to the fine art of histological preparations and always being around when I needed some help with demanding samples.

Alexandra Pacureanu, Marie-Christine Zdora, Imke Greving, Felix Beckmann, Alexander Rack and Alexander Hipp for their help during synchrotron measurements. They are the prime example that being a beamline scientist requires unlimited patience and an untainted love for science. Without their work, no meaningful synchrotron data could have been collected.

- For valuable scientific collaborations that occurred during the course of this project:

Alessandro Mirone and Pierre Paleo for their help in developing the ring-artifact removal algorithm and for reconstructing large series of synchrotron datasets.

Philipp Janz for preparing large series of animal specimens and sharing his expertise on mouse brain models.

Michel Roethlisberger for initiating a collaboration and sharing his clinical expertise as a neurosurgeon.

- For offering their help, even though I did not have the chance yet to work a lot with them:

Marzia Buscema, Natalia Chicherova and Bekim Osmani for the useful scientific discussions

Willy Kuo, Anna Khimchenko, Stefan Siegrist and Emre Cörek for their help during the beamtimes

Urs Fisch and Christian Schneider for helping me to significantly improve the study proposal.

Arnaud Scherberich for providing me with the biopsy punches essential for specimen preparation.

Stefan Gentsch and Sascha Martin for their top-quality work in fabricating dozens of specialized sample holders on a short notice for both of our laboratory  $\mu$ CT systems.

On a personal level, I would like to thank my girlfriend, Aggeliki for her wise advice whenever I asked for it, her endless patience and support when I needed it, and most importantly, her love on all the bad and the good days alike. I am so lucky to have you in my life and I love you more than you can imagine.

I would not have been here were it not for my parents, who have dedicated their life to the upbringing and education of their children. For as long as I remember they were there for my brothers and me and by their example they have taught us the virtues of truth, honesty and hard work. I only hope I can be as good a parent to my children as you have been for me.



# Curriculum Vitae

**Family Name:** Bikis  
**First Name:** Christos  
**Citizenship:** Greece  
**Professional Address:** Psychiatric University Clinic Zürich  
Lenggstrasse 31  
8032 Zürich  
**Date of Birth:** 04.08.1987  
**Place of Birth:** Athens, Greece

## Education

- 2015–2017** MD-PhD in Experimental Physics  
University of Basel (Prof. B. Müller)  
Basel, Switzerland
- 2011–2014** Bachelor of Science Physics  
Swiss Federal Institute of Technology Zürich  
Zürich, Switzerland
- 2005–2011** Medical Degree  
National and Kapodistrian University  
Athens, Greece
- 2002–2005** High School  
Doukas College  
Athens, Greece

## Professional Experience

- 2018–present** Resident  
Psychiatric University Clinic Zürich  
Zürich, Switzerland
- 2015–2017** Research Assistant  
Medical Faculty, University of Basel  
Basel, Switzerland
- 2009–2011** Research Fellow  
Medical Faculty, National and Kapodistrian University  
Athens, Greece